NAVAL POSTGRADUATE SCHOOL

MONTEREY, CALIFORNIA

THESIS

DOUBLE-DIFFUSIVE CONVECTION IN ROTATIONAL SHEAR

by

James S. Ball

March 2015

Thesis Advisor: Timour Radko
Second Reader: John Colosi

Approved for public release; distribution is unlimited

THIS PAGE INTENTIONALLY LEFT BLANK

REPORT DOCUMENTATION PAGE

Form Approved OMB No. 0704–0188

1. AGENCY USE ONLY *(Leave blank)*	2. REPORT DATE	3. REPORT TYPE AND DATES COVERED
	March 2015	Master's Thesis

4. TITLE AND SUBTITLE
DOUBLE-DIFFUSIVE CONVECTION IN ROTATIONAL SHEAR

5. FUNDING NUMBERS

6. AUTHOR(S) James S. Ball

7. PERFORMING ORGANIZATION NAME(S) AND ADDRESS(ES)
Naval Postgraduate School
Monterey, CA 93943-5000

8. PERFORMING ORGANIZATION REPORT NUMBER

9. SPONSORING /MONITORING AGENCY NAME(S) AND ADDRESS(ES)
N/A

10. SPONSORING/MONITORING AGENCY REPORT NUMBER

11. SUPPLEMENTARY NOTES The views expressed in this thesis are those of the author and do not reflect the official policy or position of the Department of Defense or the U.S. Government. IRB Protocol number ____N/A____.

12a. DISTRIBUTION / AVAILABILITY STATEMENT
Approved for public release; distribution is unlimited

12b. DISTRIBUTION CODE

13. ABSTRACT (maximum 200 words)

This study examined the effect a variety of induced velocity shears had on salt finger formation. Two harmonic, single frequency velocity profiles were utilized under varied shear strength and angular frequency. The third multi-frequency experiment employed a stochastic shear wave field. This model used frequencies that conformed to the GM spectral model for internal waves with an initial random phase distribution, modeling an environment representative of typical oceanic conditions. These shear profiles were incorporated in a double diffusion numerical model. The model resolved the formation and development of salt fingers and recorded the resultant salt and heat fluxes. The results showed that shear strength and direction influenced salt finger diffusion rates and structure alignment. For a stochastic environment, this effect is driven largely by near-inertial motions. The low-frequency waves align salt fingers, and the wax and wane of these waves impact the instantaneous diffusive rates. These internal waves reduced the salt and heat flux to that representative for un-sheared two-dimensional double diffusion simulation.

14. SUBJECT TERMS
Double Diffusion, Salt Fingers, Density Ratio, Richardson Number, Direct Numerical Simulation, Dimensional Analysis, Garret-Munk, Stochastic Shear

15. NUMBER OF PAGES
73

16. PRICE CODE

17. SECURITY CLASSIFICATION OF REPORT	18. SECURITY CLASSIFICATION OF THIS PAGE	19. SECURITY CLASSIFICATION OF ABSTRACT	20. LIMITATION OF ABSTRACT
Unclassified	Unclassified	Unclassified	UU

NSN 7540–01-280-5500

Standard Form 298 (Rev. 2–89)
Prescribed by ANSI Std. 239–18

THIS PAGE INTENTIONALLY LEFT BLANK

Approved for public release;distribution is unlimited

DOUBLE-DIFFUSIVE CONVECTION IN ROTATIONAL SHEAR

James S. Ball
Lieutenant, United States Navy
B.S., University of New Mexico, 2007

Submitted in partial fulfillment of the
requirements for the degree of

MASTER OF SCIENCE IN PHYSICAL OCEANOGRAPHY

from the

NAVAL POSTGRADUATE SCHOOL
March 2015

Author: James S. Ball

Approved by: Timour Radko
Thesis Advisor

John Colosi
Second Reader

Peter Chu
Chair, Department of Oceanography

THIS PAGE INTENTIONALLY LEFT BLANK

ABSTRACT

This study examined the effect a variety of induced velocity shears had on salt finger formation. Two harmonic, single frequency velocity profiles were utilized under varied shear strength and angular frequency. The third multi-frequency experiment employed a stochastic shear wave field. This model used frequencies that conformed to the GM spectral model for internal waves with an initial random phase distribution, modeling an environment representative of typical oceanic conditions. These shear profiles were incorporated in a double diffusion numerical model. The model resolved the formation and development of salt fingers and recorded the resultant salt and heat fluxes. The results showed that shear strength and direction influenced salt finger diffusion rates and structure alignment. For a stochastic environment, this effect is driven largely by near-inertial motions. The low-frequency waves align salt fingers, and the wax and wane of these waves impact the instantaneous diffusive rates. These internal waves reduced the salt and heat flux to that representative for un-sheared two-dimensional double diffusion simulation.

THIS PAGE INTENTIONALLY LEFT BLANK

TABLE OF CONTENTS

I. INTRODUCTION 1
A. DOUBLE DIFFUSION HISTORY 1
B. DOUBLE DIFFUSION 2
1. Diffusive Convection 2
2. Salt Fingers 3
3. Theoretical Background 4
C. VELOCITY SHEAR 5

II. MODEL DESIGN 9
A. BASIC MODEL SETUP 9
B. VERSIONS OF THE BASIC MODEL 11
1. Non-sheared Simulations 11
2. Single-frequency, Unidirectional Shear 12
3. Single-Frequency, Rotational in Space, Shear 14
4. Stochastic Shear 15

III. RESULTS: SINGLE FREQUENCY SHEAR 21
A. NON-SHEARED SIMULATIONS 21
B. STEADY SHEAR SIMULATIONS 25
C. ADJUSTING THE PERIOD OF ROTATION 30
1. Rotational Velocity Shear Under $R_i = 0.5$ 31
2. Rotational Velocity Shear Under $R_i = 2$ 33

IV. RESULTS: STOCHASTIC SHEAR 39
A. DOUBLE DIFFUSION UNDER AN UNFILTERED FREQUENCY TIME SERIES 39
B. DOUBLE DIFFUSION UNDER FILTERED FREQUENCY TIME SERIES 42

V. CONCLUSIONS 47
A. VARYING RICHARDSON NUMBER 47
B. VARYING FREQUENCY 47
C. STOCHASTIC SHEAR 48
D. NAVAL RELEVANCE 49

APPENDIX 51

LIST OF REFERENCES 53

INITIAL DISTRIBUTION LIST 55

THIS PAGE INTENTIONALLY LEFT BLANK

LIST OF FIGURES

Figure 1. Simplified illustration depicting the mechanics of salt fingering (from Ruddick and Kerr 2003)..... 4
Figure 2. The unidirectional single-frequency shear profile used during the second model version of the research..... 12
Figure 3. The velocity shear profile used during the third version of the model..... 15
Figure 4. The unfiltered frequencies from the GM spectral model. The filtered frequency cutoff points are shown as f_1 and f_2 18
Figure 5. Stochastic velocity shear time series generated Figure 4..... 18
Figure 6. Stochastic velocity time series generated from Figure 4. 19
Figure 7. The dimensional u velocity shear time series generated following the implementation of low-pass, band-pass, and high-pass frequency filters are shown in red. These are shown relative to the unfiltered velocity shear time series shown in black. 20
Figure 8. The baseline three-dimensional double diffusion simulation at time step 116 without induced velocity shear. 22
Figure 9. A magnified (2X) view of the baseline three-dimensional double diffusion simulation at time 116 without induced velocity shear..... 22
Figure 10. The baseline three-dimensional double diffusion simulation shown from the visualization software VAPOR..... 23
Figure 11. The two- and three-dimensional baseline reference values (non-dimensional units) for double diffusion without velocity shear. 24
Figure 12. The initiation of salt fingers during the simulation using the version two non-rotational shear model for $R_i = 2$ 25
Figure 13. Fully developed salt fingers during the simulation using the version two non-rotational shear model for $R_i = 2$ 26
Figure 14. Salt finger structure from the simulation using the version two non-rotational shear model for $R_i = 2$. This shows the same time step from viewpoints offset by $90°$ to show impact from u and v velocity on salt finger structure. 26
Figure 15. Initial salt finger development during the simulation using the version three non-rotational shear model for $R_i = 2$ 27
Figure 16. The version three non-rotational shear profile for $R_i = 2$, showing salt finger structure alignment from the dominate shear. This shows the same time step at viewpoints offset by $90°$, to show impact of u and v velocity shear on salt finger structure. 28
Figure 17. Salt finger structure during the version three non-rotational shear model for $R_i = 2$ after ~60 hours of real time. 29
Figure 18. Mean temperature fluxes after stabilization between model versions two and three's non-rotational velocity profiles for each value of

Richardson number. This is referenced to the baseline three-dimensional heat flux without velocity shear..... 30
Figure 19. The version three shear model simulation for $R_i = 0.5$ and a period of rotation of four hours. 32
Figure 20. Salt finger initiation during the version two shear model simulation for $R_i = 2$ and a period of rotation of four hours. 34
Figure 21. Fully developed salt fingers from the version two shear model for $R_i = 2$ and a period of four hours. 34
Figure 22. The impact of shear on salt finger structure during the version three shear profile for $R_i = 2$ and a period of four hours. 35
Figure 23. The impact of shear on salt finger structure during the version three shear profile for $R_i = 2$ and a period of four hours. This shows that the structure of salt fingers re-align as the direction of shear changes. 36
Figure 24. The simulation of version three shear model for $R_i = 2$ and a period of rotation of four hours. This showed the additional instabilities that contributed to the vertical transport of salt and heat. 37
Figure 25. Double diffusion salt finger flux under the unfiltered GM frequency generated stochastic velocity shear time series. This is compared to the mean baseline two-dimensional double diffusion rates. 40
Figure 26. The initiation of salt finger development under the unfiltered stochastic velocity shear..... 41
Figure 27. Salt finger structure alignment during a period of reduced velocity shear in the simulation of unfiltered stochastic velocity shear. 41
Figure 28. The correlation of $r_{fl}(t)$ and $-r_{sh}(t)$ from the unfiltered stochastic shear simulation. 42
Figure 29. Salt fingers during the simulation for a low-pass filtered frequency generated stochastic velocity shear..... 43
Figure 30. Salt fingers during the simulation for a band-pass filtered frequency generated stochastic velocity shear..... 44
Figure 31. Temperature flux from the filtered stochastic velocity shear simulations compared to the baseline two- and three-dimensional temperature flux with zero velocity shear. 45
Figure 32. The influence from velocity shear on salt finger structure alignment during the stochastic velocity shear simulations. From left to right the figures represent shear from; unfiltered frequency forcing, low frequency filtered forcing, intermediate filtered frequency forcing, and high filtered frequency forcing. 46

LIST OF TABLES

Table 1. The complete results from the version one baseline model of two- and three-dimensional double diffusion models without velocity shear. 24

Table 2. The full resultant mean flux from the version two and three non-rotational shear models after stabilization has occurred. 30

Table 3. The simulation results from the rotational part of model versions two and three for $R_i = 0.5$. 33

Table 4. The simulation results from the rotational part of model versions two and three for $R_i = 2$. 37

Table 5. The resultant double diffusion salt and heat flux from each stochastic velocity shear time series simulation. 44

Table 6. Base DNS model inputs 51

THIS PAGE INTENTIONALLY LEFT BLANK

LIST OF ACRONYMS AND ABBREVIATIONS

DNS	direct numerical simulation
HPCMP	High Performance Computing Modernization Program
TACC	University of Texas at Austin's Advance Computing Center
DOD	Department of Defense
XSEDE	Extreme Science and Engineering Discovery Environment
GM	Garrett-Munk
RMS	Root Mean Square
WBK	Wentzel-Kramers-Brillouin

THIS PAGE INTENTIONALLY LEFT BLANK

ACKNOWLEDGMENTS

First, I must thank my loving and supportive wife, Amy, and daughters Makenna and Sydney. Amy's daily support and encouragement has been instrumental to my success at the Naval Postgraduate School in Monterey. I will never forget the feeling of being able to come home every day to their open arms and the sound of "Daddy's Home"!

I would like to thank my advisor, Dr. Timour Radko, for his guidance, patience, wealth of knowledge and dedication to this project. His unwavering enthusiasm and intellectual expertise for both the subject and model simulation are the reason for this project's success.

I also would like to thank Dr. Jason Flanagan. I had minimal experience with computer simulations prior to this research. His expertise in Linux, computer programming, and MATLAB was the cornerstone of this research. Never once did he turn me away when I would approach and say "So, I have this problem." Instead he would laugh and help me understand how I got there and how to could avoid a similar situation in the future.

I am deeply grateful to John Colosi who helped me understand all things Garrett-Munk. Without his assistance, the final shear profile version for this research might not have been achieved.

Last, I would like to thank all my friends, family, and the Naval Postgraduate School. Each contributed in some way to make this tour successful and enjoyable. I am deeply grateful for the opportunity to expand my knowledge both professionally and academically. The memories and friends obtained here will last a lifetime.

THIS PAGE INTENTIONALLY LEFT BLANK

I. INTRODUCTION

To fully understand double diffusion and the impact of current and future research, several studies were considered. The first study investigated the relevant historic research about the discovery of double diffusion. Next, a study was conducted on the various methods of double diffusion, when each method could occur, and the governing theory behind each method. After this basic familiarization, a study on the particular area of research was pursued.

A. DOUBLE DIFFUSION HISTORY

The Earth's ocean is affected by a broad range of large- and small-scale processes. One small-scale ocean process is double diffusion. A number of fundamental processes in oceanography and beyond are controlled by stratification, involving interaction between areas with different concentrations of a specific property or components. The rate these properties mix can vary based upon their respective molecular diffusivities. The mixing process a liquid undergoes when composed of two properties of differing molecular diffusivities is known as double diffusion. In 1857, W. Stanley Jevons conducted an experiment to model cirrus clouds. One result from this experiment was a process called "sugar fingering" and closely aligns with current "salt fingering" research (Schmitt 1995).

The sugar fingering phenomenon was noted in the results of the experiment, but no strong interest on the subject occurred for approximately one hundred years (Schmitt 1995). An experiment by Stommel, Arons and Blanchard (1956) to determine deep ocean pressure resulted in a discovery they named the "Perpetual Salt Fountain." A thermally conductive vertical pipe connected a deep layer of cold less saline water with an upper layer of warm water with a higher salt content. As the temperatures of the layers equalized, water issued from the pipe as the water density of the bottom layer dropped below density for the upper layer (Stommel, Arons and Blanchard 1956). Melvin Stern (1960) took these

findings a step further when he established that the two-order of magnitude difference in thermal diffusion relative to the diffusivity of salt can drive intense small-scale instability known as double-diffusive convection (Stern 1960).

B. DOUBLE DIFFUSION

Temperature is the main diffusive component affecting fresh water density. With the exception of water at just above freezing temperature, water density increases as the temperature decreases. When warm water lies above cold water, the water density increases with depth, and the water column is stable. Initial forces acting on this volume of water has a dampened effect from the gravitational potential energy of the density gradient and results in minimal mixing. In an isothermal water volume, the water density is relatively constant with depth. This is also stable and the same force acting on the water column would have an increased impact from the reduced dampening force caused by the missing density gradient. Density decreases with depth if cold water lies over warm water. This water column is unstable and the difference in potential energy from the surface and the bottom would provide the sufficient energy to cause overturning and mixing of the fluid column.

The concept of stability is more complex for the ocean. In seawater, both temperature and salt content or salinity significantly impact water density. Stern established the diffusion rate for temperature is approximately 100 times the rate of salt diffusivity (1960). This difference in diffusion rates and the resulting effect on density is the key component for double diffusion theory. As a result, a volume of water in the ocean with density increasing with depth may not be considered stable until double diffusion has been accounted for (Stern 1960).

1. Diffusive Convection

Diffusive convection can occur when a layer of cold fresh water is above a warm salty layer (Stern 1960). Turner and Stommel demonstrated how this diffusive convection process could occur (1964). An initial external force such as a pressure wave or an object in the water displaces a small volume of cold water

downward into the warm layer while maintaining the original salinity. The resultant heat gain caused the density of the water volume to drop lower than the surrounding fluid and subsequently rise back in the water column (Turner and Stommel 1964). The water volume is less dense than it was originally and this additional buoyancy forced the water volume to overshoot the initial starting position. The reverse now occurred with the water volume now losing heat to the surrounding colder water with salt content retention and the corresponding density increase and subsequent descent in the water column. This buoyancy difference is a net gain of kinetic energy, and the volume drops below the previous low level (Turner and Stommel 1964). As the process repeats, the net energy gain each cycle translates to an increase in oscillation amplitude to over time. This is similar to the opposite effect in oscillation from a dampening spring. The increase in oscillation causes the water to become more turbulent and a gradual mixing of salt and temperature occurs in the water column (Turner and Stommel 1964).

2. Salt Fingers

The double diffusion method known as “salt fingering” occurs when a warm salty layer lies above a cold fresh layer (Stern 1960). A small parcel of warm water transfers heat to the colder layer, and water density increases. This causes the parcel of water to descend in the water column while maintaining its original salinity (Stern 1960). As the parcel of water descends, the surrounding water temperature is also lower, and further heat transfer takes place with the additional increase in density. This descending volume of water creates a trailing tendril of higher salinity water that elongates into the lower layer (Stern 1960). These “salt fingers” are only a few centimeters in width and extend to a few decimeters in length (Schmitt 1994). The reverse effect occurs as a parcel of cold water gains heat from the above layer. These salt fingers result in a slow mixture of heat and salinity between the two layers (Stern 1960). This salt finger process is illustrated in Figure 1.

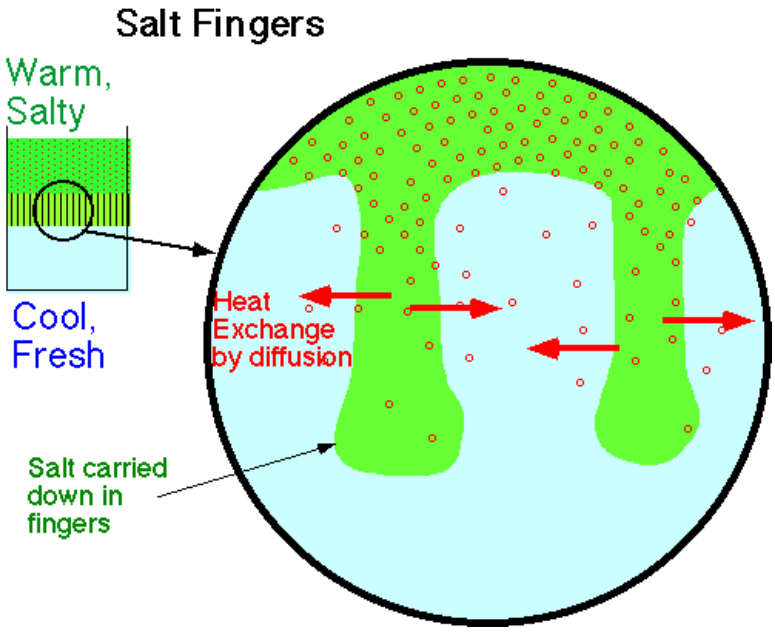

Figure 1. Simplified illustration depicting the mechanics of salt fingering (from Ruddick and Kerr 2003).

3. Theoretical Background

The two methods of double diffusion occur when the density ratio R_ρ is within a specific range for each method. The density ratio is a relationship of the thermal expansion coefficient α and temperature gradient T_Z in comparison to the saline expansion coefficient β and salinity gradient S_Z.

$$R_\rho = \frac{\alpha T_Z}{\beta S_Z} \tag{1.1}$$

$$\begin{aligned} &\text{for salt fingering,} && 1 < R_\rho < \frac{1}{\tau} \\ &\text{for diffusive convection,} && 1 < R_\rho^* = R_\rho^{-1} < \frac{P_r + 1}{P_r + \tau} \end{aligned} \tag{1.2}$$

$$P_r = \frac{\upsilon}{k_T} \tag{1.3}$$

If the density ratio is less than one, double diffusion will not occur in the water column. With ocean diffusivity ratio $\tau \approx 0.01$, the allowable range for salt finger

formation is $\left(1 < R_\rho < 100\right)$ (Radko 2013). This density ratio range exists in many regions of the ocean, particularly in the mid- latitude Atlantic thermocline (Schmitt, 1994). The relative strength for salt finger mixing is a factor of the density ratio. The relative strength of salt fingers is high with a low R_ρ and weak with a high R_ρ (Radko 2013).

The Prandtl number P_r is a factor of the viscous diffusion rate υ, and thermal diffusion rate α and is a measure in determining favorable conditions for diffusive convection. This causes the range for diffusive convection in the ocean to be considerably narrower $\left(1 < R_\rho^{-1} <\approx 1.07\right)$. As a result, a much smaller portion of the ocean has favorable conditions for diffusive convection. The common measure of double diffusive convection is the flux ratio γ of the molecular flux of temperature F_T and salt F_S.

$$\gamma = \frac{\alpha F_T}{\beta F_S} \tag{1.4}$$

This measures the amount of potential energy transfer occurring between the two layers (Radko 2013).

C. VELOCITY SHEAR

Simple salt finger experiments have been conducted in a column of water devoid of current flow. Huppert and Turner (1981) conducted a simple laboratory experiment with a stable temperature gradient and poured a salt solution on top to create the salt gradient. This experiment resulted in a salt finger structure that was aligned with the vertical axis. This laboratory environment doesn't exist in the ocean that is continually under the influence of many internal waves of varying frequency. This results in a wide range of velocity shears. This shear has been hypothesized to be disruptive to salt finger formation or elongation (Stern 1969). Velocity shear is this study will refer the difference in velocity between separate points in the water column. Linden (1974) conducted a physical

experiment to determine whether salt fingers could exist under steady velocity shear conditions. The experiment ran for a variety of Richardson numbers R_i with a steady velocity shear. Linden concluded salt fingers could form under these conditions and estimated that thermal and salt flux was not significantly reduced as a result of the steady shear (1974). The salt finger structures observed during the experiments were aligned by the shear, and Linden hypothesized salt fingers in the ocean would follow a similar alignment by the mean current flow.

$$R_i = \frac{N^2}{S^2} = \frac{\frac{g}{\rho_0}\frac{dp}{dz}}{\left(\frac{\partial u}{\partial z}\right)^2 + \left(\frac{\partial v}{\partial z}\right)^2} \tag{1.5}$$

Kunze et al. (1998) took shadowgraphs of several small scale laminae near Barbados and found them to be tilted within 10 degrees of horizontal. While conducting the North Atlantic tracer release experiment, St. Laurent and Schmitt (1990) found areas with favorable conditions for salt fingers. The developed salt fingers were tilted 10–20 degrees from horizontal. The shear from these experiments is significantly more complex from the simple sear induced by Linden. Despite this difference in complexity, these results agree with the hypothesis proposed by Linden for open ocean salt finger structure (Linden 1974).

Establishing laboratory conditions to study salt fingers under a wide array of adjustable conditions is very difficult. The development of stratified layers often incorporates some type of permeable membrane. This can lead to additional difficulties in measuring salt and heat flux and accounting for the thermal transfer capability of the membrane. Another significant problem is the establishment of shear conditions and trying to mimic conditions found in the ocean, where ocean currents can vary direction over time. Lengthy experiments would also require a large reservoir to maintain the chemical stratification necessary.

The solution for these difficulties is the use of direct numerical simulations (DNS). The use of DNS modeling allows accurate measurements at any location within the model at any given point in time. Without the use of artificial membranes to setup the model, limitations for generating shear or the inclusion of physical boundary conditions, the model is able to perform more in accord with actual oceanic conditions. Kimura and Smyth (2007) conducted DNS experiments of salt sheets and turbulence in a double diffusive shear layer. The formation of salt sheets from the DNS was consistent with results from Linden (1974). These salt sheets were aligned with the predominate shear, examination of the cross-flow direction revealed vertical salt finger development similar to non-sheared environments. The diffusivity of salt K_S was found to increase exponentially until secondary instability began. The diffusivity then followed a rapid reduction to a stable value. The end stability point for K_S was significantly lower than values estimated without shear (Kimura and Smyth 2007). This would suggest shear has a larger impact on double diffusion rates than initially theorized.

These simulations and experiments looked at steady shear conditions. The question remained for how salt finger double diffusion would be impacted from internal waves in the ocean. These wave patterns experience a wax and wane effect and are multi-directional in nature. Kunze (1990) and Radko (2013) questioned whether this continual shift in orientation and strength of shear could suppress salt fingers in all directions, an effect termed isotropic suppression. Oceanic shear is largely derived from near-inertial waves and timescales approximating a day. The salt finger development timescale is much shorter, on the order on minutes. This difference in timescale would mean that instantaneous shear from the near-inertia component would be quasi-steady. Higher frequency waves are less energetic but with a timescale more comparable to salt finger formation. This research will examine the effect that a range of frequencies has upon salt finger formation.

One of the principal components for velocity shear in the ocean are internal waves. Garrett and Munk (1972) developed an empirical spectral model used to understand oceanic internal waves. The original formula has been updated several times to try and address difficulties with comparing internal waves under different conditions. Some geophysical configurations introduce inconsistencies which have been reported for extreme high or low latitudes and coastal regions. Outside of these regions, the GM spectral model is useful for broad spectrum understanding of internal waves in the ocean. The use of the GM spectral model allows for a simple description of internal wave energy from buoyancy frequency to Coriolis (Munk 1981).

II. MODEL DESIGN

The use of numerical modeling is a generally accepted, straightforward means for computing double diffusion mix rates. The computer model used in this research is based on a de-aliased pseudo-spectral method. This model was initially used by Stern and Radko for two- and three-dimensional salt-finger simulations (1999). The model utilizes C and Fortan compilers to implement the C subroutine library, FFTW, to compute discrete Fourier transforms in multi-dimensional analysis. The model supports a parallel input/output (I/O) interface for data transfer through a Message Passing Interface (MPI) algorithm. This allows for computationally intensive multi-dimensional analysis without the corresponding increase in physical time to conduct the simulation through the employment of multiple computer processors (Stern and Radko 1999).

The DOD supercomputing resources of Cray Xe6 Garnet accessible through HPCMP, and the civilian supercomputing resources from the XSEDE program at the University of Texas were used during this research. Each simulation used the parallel processing power of 512 or 1024 computer core resources from one of these two facilities. This processing power allowed for a large increase in resolution yet permitted the simulation run-time to remain reasonable. The more complex computationally intensive simulations required in excess of 73,000 effective computer run-hours each to complete. The use of parallel processing reduced this simulation run time from 8.4+ years on a standalone desktop computer to a calendar week to complete.

A. BASIC MODEL SETUP

The model operates under single precision and model parameters were chosen to represent the Atlantic Thermocline. A diffusivity ratio τ=0.01, Prandtl number $P_r = 7$ and density ratio $R_\rho = 2$ were used. The simulation dimensions are an unbounded box of $L_x = 50$, $L_y = 50$ and $L_z = 100$, resolved into $N_x = 384$,

$N_y = 384$ and $N_z = 768$ computational elements. Temperature and salinity are separated into their respective uniform background gradients $\overline{T}$ and $\overline{S}$ and the departure T and S from this gradient. Favorable background stratification for salt finger development is $\overline{T}_Z > 0$ and $\overline{S}_Z > 0$. The model uses the Boussinesq equations of motion with the linear equations of state, are expressed in terms of the perturbation of T and S. The scale for temperature and salinity perturbations is $\alpha \overline{T}_Z l$. These equations were then non-dimensionalized by length, time, velocity and pressure.

$$\begin{aligned} &\text{length} && \left(\frac{k_T \upsilon}{g\alpha \overline{T}_Z}\right)^{1/4} \\ &\text{time} && \frac{l^2}{k_T} \\ &\text{velocity} && \frac{k_T}{l} \\ &\text{pressure} && \frac{\rho_0 \upsilon k_T}{l^2} \end{aligned} \tag{2.1}$$

where k_T, k_S are the molecular diffusivities of heat and salt, υ is the kinematic viscosity, g is acceleration from gravity, α is the thermal expansion coefficient, $\overline{T}_Z$ is the nominal background temperature gradient, H is the domain height and ρ_0 is the reference density from the Boussinesq approximation.

$$\overline{T}_Z = \frac{\left(T_{top} - T_{bottom}\right)}{H} \tag{2.2}$$

The resultant non-dimensionalized equations for the model are:

$$\frac{1}{P_r}\left(\frac{\partial}{\partial t}\vec{v} + \vec{v}\cdot\nabla\vec{v}\right) = -\nabla p + \left(T - S\right)\vec{k} + \nabla^2\vec{v} \tag{2.3}$$

$$\nabla\cdot\vec{v} = 0 \tag{2.4}$$

$$\frac{\partial T}{\partial t} + \vec{v}\cdot\nabla T + w = \nabla^2 T \tag{2.5}$$

$$\frac{\partial S}{\partial t} + \vec{v} \cdot \nabla S + \frac{w}{R_\rho} = \tau \nabla^2 S \tag{2.6}$$

where $\vec{v} = (u, v, w)$ is the velocity vector and $\vec{k}$ is the vertical unit vector. Periodic boundary conditions were assumed for each spatial direction and integrated with the governing equations using the de-aliased pseduospectral method (Stern et al. 2001, Stellmach et al. 2011). Vertical shear was introduced from the amplitude of the spectral component (u, v) to be fundamental in z and uniform in (x, y) for the Fourier component (0,0,1). The model then used the Prandtl number P_r, the density ratio R_ρ and the molecular diffusivity ratio $\tau = \frac{k_S}{k_T}$ to determine how the system evolved during the simulation.

B. VERSIONS OF THE BASIC MODEL

This research was based on four separate versions of the pseudo-spectral model. Version one established baseline reference values and included a two- and three-dimensional non-sheared double diffusion mode. The second version introduced a unidirectional single frequency shear that was also rotational in time about the vertical axis. The third version used a single-frequency shear that was rotational in space and time about the vertical axis. The final version incorporated a stochastic shear profile to simulate open ocean conditions.

1. Non-sheared Simulations

Two reference non-sheared simulations were performed. The first simulation used a two-dimensional double diffusion model in the x and z plane of reference. The second simulation utilized the three-dimensional model that was also used for model versions two through four, but under zero shear conditions. The base simulation model results were used for comparison and validation for the latter stages of this research.

2. Single-frequency, Unidirectional Shear

The second model version utilized a unidirectional single-frequency shear that was rotational in time about the vertical axis. A single time-step of the shear profile is shown in Figure 2. In this figure, the blue vector arrows radiating from the z axis indicate the direction and magnitude of the current at each vertical height. The first part of the analysis examined double diffusion under different peak amplitudes of this wave with zero angular rotation. The second part held the peak amplitude constant and introduced different angular frequencies into the rate of rotation. The shear profile then rotated about the vertical red-dashed line at the specified angular frequency.

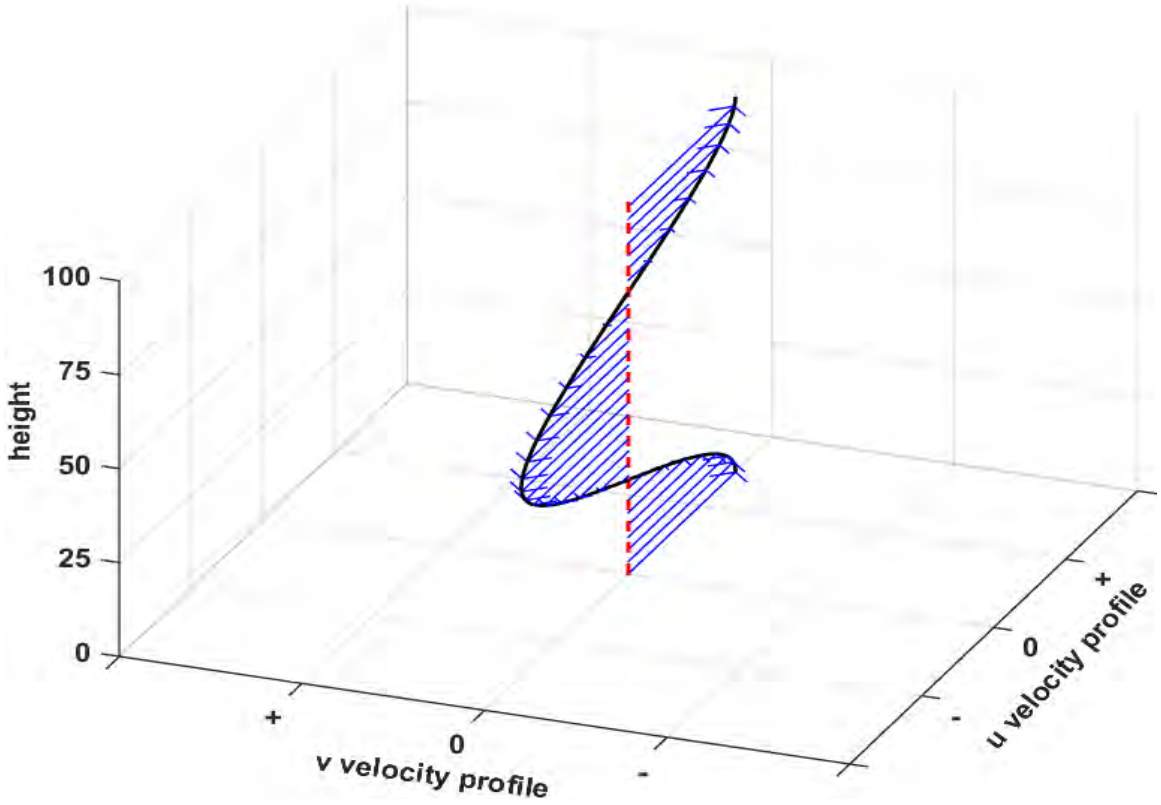

Figure 2. The unidirectional single-frequency shear profile used during the second model version of the research.

The Figure 2 shear profile used $m = \frac{2\pi}{L_z}$ as the vertical fundamental wavenumber. This shear profile is a unidirectional shear that was derived from the harmonic:

$$\begin{aligned} u_{001} &= A\cos(\omega t)\cos(mz) \\ v_{001} &= -A\sin(\omega t)\cos(mz) \end{aligned} \tag{2.7}$$

where A is the peak amplitude and ω is the angular frequency of rotation. The peak amplitude was determined by from the prescribed Richardson number R_i. After non-dimensionalization and the substitution of base components, the equation relating A and R_i has been obtained.

$$R_i = \frac{\frac{g}{\rho_0}\frac{dp}{dz}}{\left(\frac{\partial u}{\partial z}\right)^2 + \left(\frac{\partial v}{\partial z}\right)^2} = P_\Gamma \frac{\left(1 - \frac{1}{R_\rho}\right)}{m^2 A^2 \cos^2(mz)} \tag{2.8}$$

This equation is solved for A, which shows that the peak amplitude was large for low R_i and small for large R_i.

$$A = \sqrt{\frac{P_\Gamma\left(1 - \frac{1}{R_\rho}\right)H^2}{(2\pi)^2 R_i}} \tag{2.9}$$

This expression was evaluated using r $P_r = 7$, $R_\rho = 2$ and $H = 100$, and the peak velocity shear amplitudes computed for R_i values of $[0.5,\ 1,\ 2,\ 4,\ 8,\ 16,\ 32,\ 64,\ 128,\ \text{or}\ 256]$ under zero angular frequency. Such a wide set of parameters covers a range of regimes from those that are close to dynamic instability $(R_i < 0.25)$ to those that are minimally affected by shear $(R_i = 256)$.

The second series of experiments rotated this shear profile at specified angular frequencies ω. For each ω, simulations were performed for $R_i = 0.5$ and then for $R_i = 2$. This isolated the effect of single-frequency angular rotation on salt finger formation. Simulation conditions under $R_i = 0.5$ examined the parameter regime that is not far separated from dynamic instability, while $R_i = 2$ determined the effects on salt fingers under more favorable conditions for salt finger development. Angular frequencies equivalent to periods $T = 0.5,\ 1,\ 2 \text{ and } 4\ hr$ for each peak amplitude were used to test these effects

3. Single-Frequency, Rotational in Space, Shear

The model version utilized a single-frequency shear that was rotational in space and time about the vertical axis. A single shear profile is shown in Figure 3. In this figure, the blue vector arrows radiating from the z axis indicate the direction and magnitude of the current at each vertical height. The first part of the analysis examined double diffusion under different peak amplitudes of this wave with zero angular rotation. The second part held the peak amplitude constant and varied the rate of rotation. The shear profile then rotated about the vertical red-dashed line at the specified angular frequency.

The spatial and temporal rotation was incorporated into the model by assuming the following background velocity profile:

$$\begin{aligned} u_{001} &= A\cos\left(\omega t + mz\right) \\ v_{001} &= -A\sin\left(\omega t + mz\right). \end{aligned} \tag{2.10}$$

The peak amplitudes and angular frequencies tested were the same as those for the second version of the shear model. The third version of the shear model tested the effects of rotational shear in time and space on the effect of salt finger development and the resultant diffusion rates.

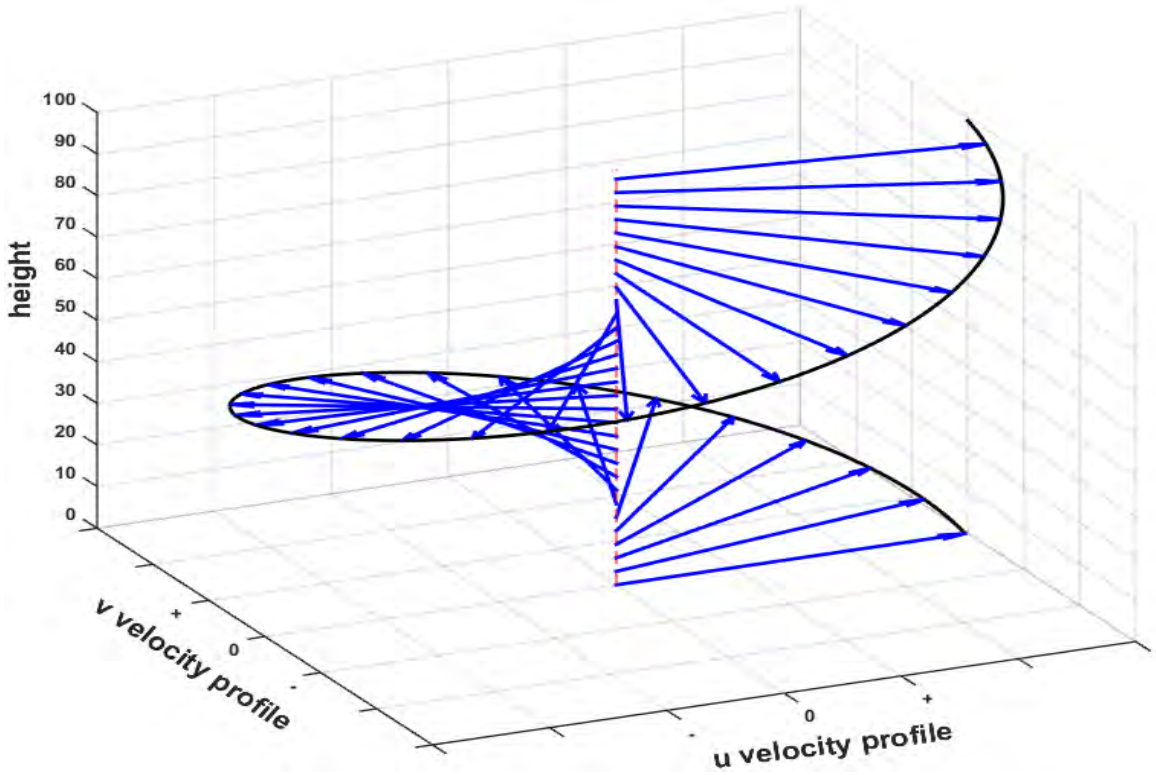

Figure 3. The velocity shear profile used during the third version of the model.

4. Stochastic Shear

The design of model versions two and three investigated the changes in double diffusion as influenced by various velocity profile strengths and different frequencies of angular rotation. The shear profile for the final model version was a multi-frequency stochastic velocity shear to best approximate the internal waves in the ocean.

An initial attempt to construct a stochastic velocity shear time series from collected data in the Caribbean and in tropical Pacific (Toole 2014, personal communication; Pinkel 2014) was attempted and led us to the conclusion that numerical modeling is the preferred method for studying problems of this nature. Data collection occurred for one-half hour as the collection vehicle dove from the surface to submergence depth. Six to eight hours then passed before a subsequent dive occurred. This time was from the combination of time to

resurface the vehicle, download the data and recharge or swap out the energy source. A continuous time series derived from these conditions would result data interpolation for more than 90 percent of the time series. The resultant time series would be insufficient for implementation into a DNS model as part of this research.

The fourth model version used a velocity shear time series profile derived from a GM frequency spectral model. A constant stratification N_o internal wave energy obeying the Garrett-Munk internal wave spectral model was assumed for this research (Munk 1981). The horizontal currents were computed as a function of time, depth and the linear sum of waves with different mode numbers j, horizontal wave numbers k and l :

$$\mathbf{u}_{\mathbf{dim}}(z,t) = \mathrm{Re}\left(\sum_{j=1}^{J} \int\int a_u(k,l,j) \cos\left(m(j)z\right) e^{i(\theta_u(k,l,j)-\sigma t)} dk dl \right) \tag{2.11}$$

$$\mathbf{v}_{\mathbf{dim}}(z,t) = \mathrm{Re}\left(-\sum_{j=1}^{J} \int\int a_v(k,l,j) \cos\left(m(j)z\right) e^{i(\theta_v(k,l,j)-\sigma t)} dk dl \right). \tag{2.12}$$

The current modes were represented by $\cos\left(m(j)z\right)$, $m = \pi j / D$, water depth D, $\tan\theta_u = fl \Big/ (-\sigma k)$, $\tan\theta_v = fl/(\sigma k)$, and Coriolis parameter f. The applied WBK dispersion relation is shown by

$$\sigma(k,l,j) = \sqrt{f^2 + N_o^2 \frac{k^2 + l^2}{m^2}} \tag{2.13}$$

Zero mean complex Gaussian random variables a_u and a_v, represent the stochastic wave amplitudes. The statistics for these was obtained from the Cartesian GM spectra

$$F_u(k,l,j) = F_\zeta(k,l,j) \frac{m^2(j)}{k^2 + l^2} f^2 \left(1 + \frac{k^2}{\hat{k}_j^2} \right) \tag{2.14}$$

$$F_v(k,l,j) = F_\zeta(k,l,j)\frac{m^2(j)}{k^2+l^2} f^2\left(1+\frac{l^2}{\hat{k}_j^2}\right) \tag{2.15}$$

$$F_\zeta(k,l,j) = \zeta_o^2 \frac{1}{N_j}\frac{1}{j^2+j_*^2}\frac{2}{\pi^2}\frac{\hat{k}_j\sqrt{k^2+l^2}}{k^2+l^2+\hat{k}_j^2}. \tag{2.16}$$

The RMS internal-wave displacement ζ_o, normalization N_j, such that $N_j^{-1}\sum_{j=1}^{J}\left(j^2+j_*^2\right)^{-1}=1$ and $\vec{k}_j = m(j)\,f/N_o$. The dispersion relation can assign wave frequencies above N_o where a_u and a_v, are set to zero. To maintain the shear variance finite, $\mathrm{R}_i = 1$ and sets the maximum mode number

$$J = \frac{D^2}{6\pi\zeta_o^2 j_*}. \tag{2.17}$$

The values used to simulate this were, $D = 1000\ m,\ N_o = 3\ cph,\ f = 1/24\ cph,$ $\zeta_o = 7.3\ m,$ and $j_* = 3.$

Figure 4 shows the generated GM frequencies as referenced to $30°$ latitude. These frequencies were used to generate the stochastic velocity shear time series. Shear values were recorded for 96 hours and these time series are shown on Figure 5.

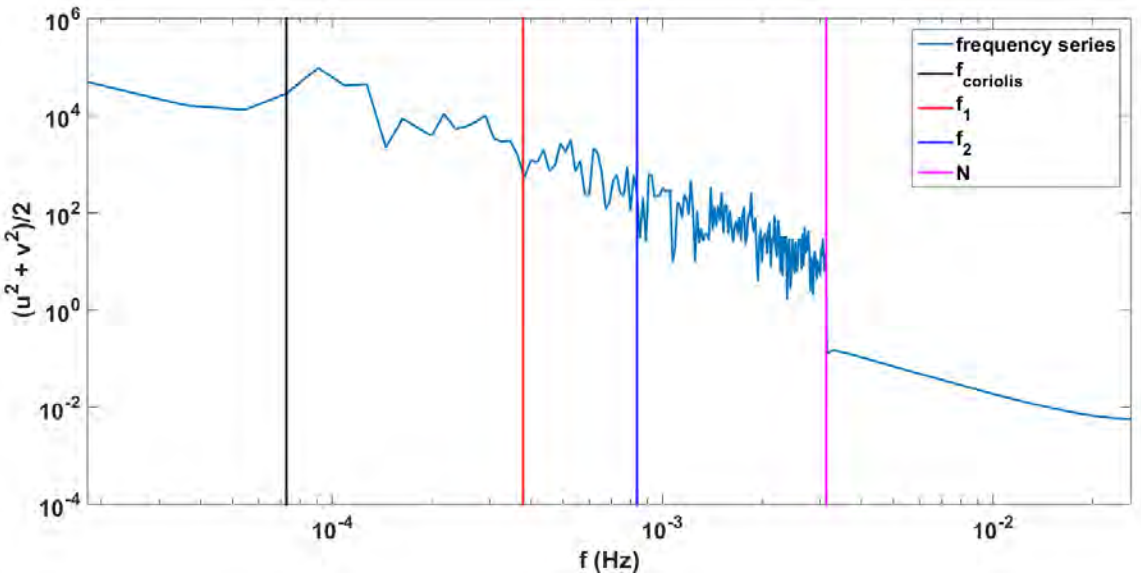

Figure 4. The unfiltered frequencies from the GM spectral model. The filtered frequency cutoff points are shown as f_1 and f_2.

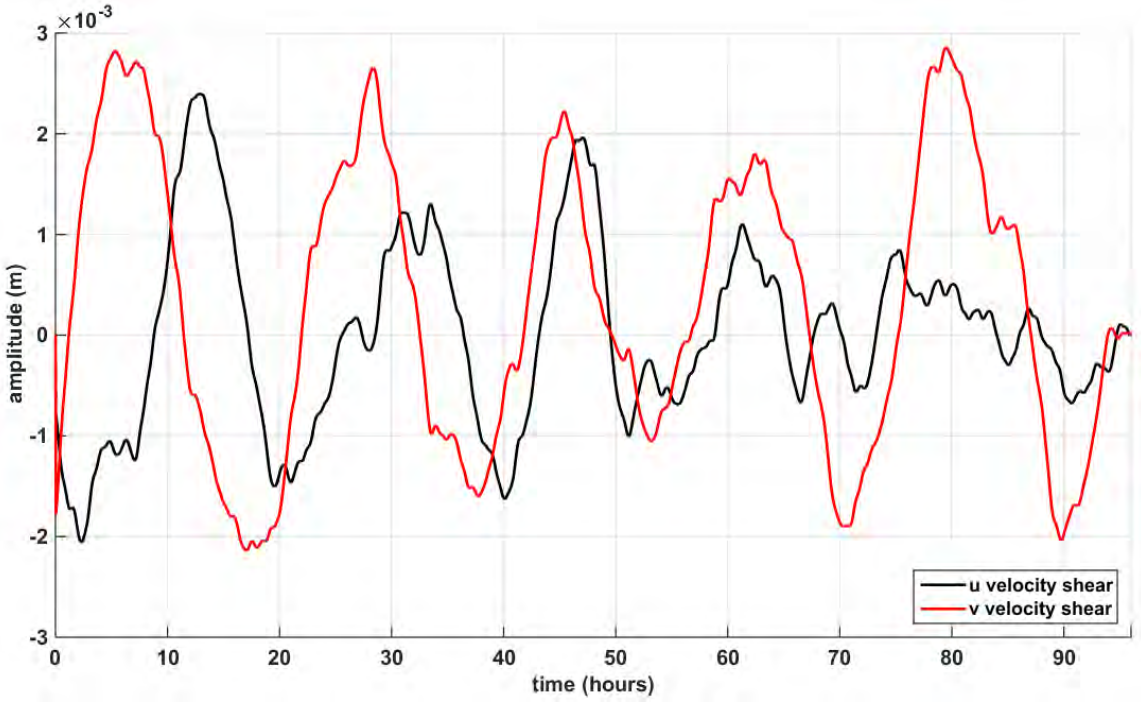

Figure 5. Stochastic velocity shear time series generated Figure 4.

The simulation occurred at a fixed vertical height (H=500m) and the simulation occurred over a finite time period (4 days). This caused small

deviations in Figure 4, but maintains the basic slope and magnitude from the theoretical GM spectral model. This time series was non-dimensionalized and introduced into:

$$u_{001} = U(t)\cos(mz)$$
$$v_{001} = V(t)\cos(mz) \tag{2.18}$$

with $U(t)=\sqrt{2}\boldsymbol{u}_z m$ and $V(t)=\sqrt{2}\boldsymbol{v}_z m$. This ensured the computed rms shear matched the small-scale model rms shear. This is similar to the single frequency analysis from part two of the version two and three shear model simulations. The generated velocity time series are shown in Figure 6.

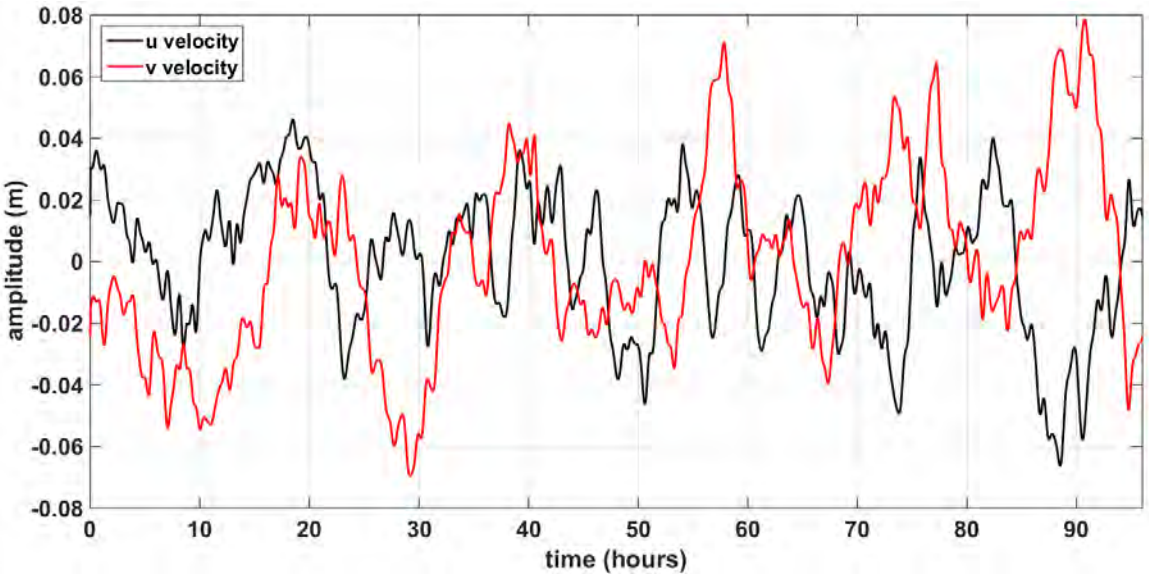

Figure 6. Stochastic velocity time series generated from Figure 4.

A set of filters was used on the original frequencies from the GM frequency spectral model to determine the effect on salt fingers from more localized frequency ranges. These frequency ranges were based on f_1 and f_2 as calculated from equation 2.9 and shown in Figure 4.

$$f_1 = f + 0.1*(N - f)$$
$$f_2 = f + 0.25*(N - f) \tag{2.19}$$

A low pass filter isolated the low range frequencies $\omega < f_1$. A band-pass filter isolated intermediate range frequencies $f_1 < \omega < f_2$. A high-pass filter isolated high range frequencies $\omega > f_2$. These individual frequency components were isolated by Fourier-transforming the shear time series into the frequency domain and implementing the respective filters. Figure 7 shows the relationship of the three filtered u velocity shear time series against the original unfiltered u velocity shear time series.

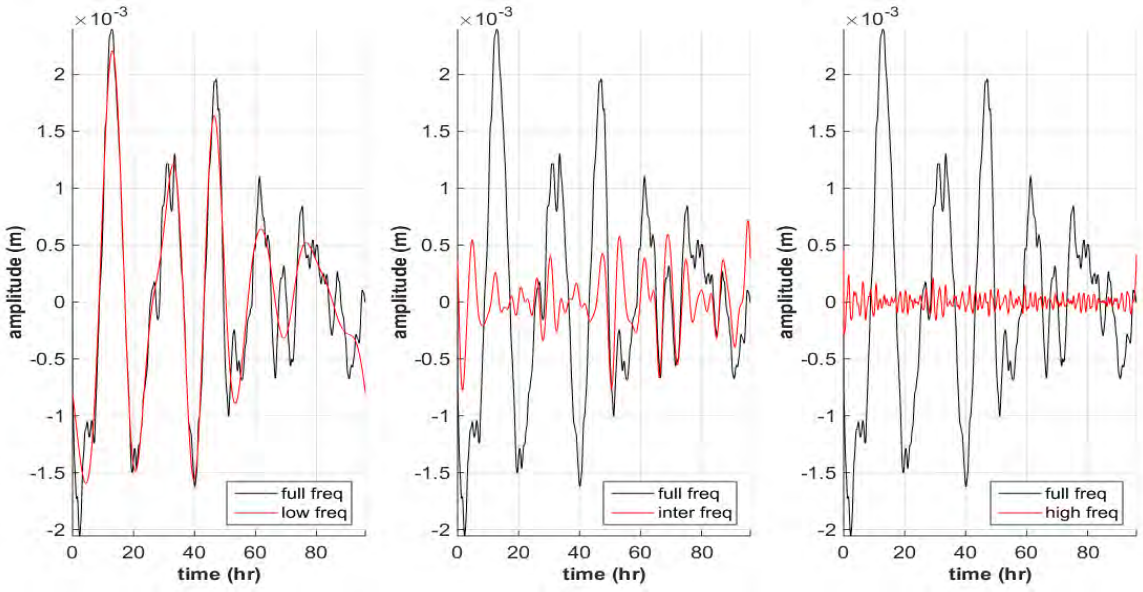

Figure 7. The dimensional u velocity shear time series generated following the implementation of low-pass, band-pass, and high-pass frequency filters are shown in red. These are shown relative to the unfiltered velocity shear time series shown in black.

III. RESULTS: SINGLE FREQUENCY SHEAR

The following are the results from the model versions one, two and three. The baseline results from version one are used to compare the results obtained from versions two and three. This analysis determined the effects of shear strength and angular rotation rate on the formation of salt fingers and the resultant heat and salt fluxes. The results for zero and finite angular frequencies are compared against each other and the baseline results.

A. NON-SHEARED SIMULATIONS

The baseline two- and three-dimensional simulations ran without influence from shear. Two-dimensional double diffusion limited the degrees of freedom a salt finger could travel as it elongates and resulted in lower double diffusion rates compared to the three-dimensional simulation. In Figures 8 and 9, a vertical slice of the three-dimensional baseline is shown at non-dimensional time 116. The center u and v velocities are the result of salt finger elongation and showed no dominate mean velocity pattern existed. The graph on the left graph shows the corresponding heat flux F_H and the corresponding F_S is shown on the right. The salt fingers are predominately aligned with the vertical axis. The baseline three-dimensional salt flux is shown in Figure 10 using the three-dimensional visualization software VAPOR. The structure of the salt fingers is seen to be aligned with the vertical axis.

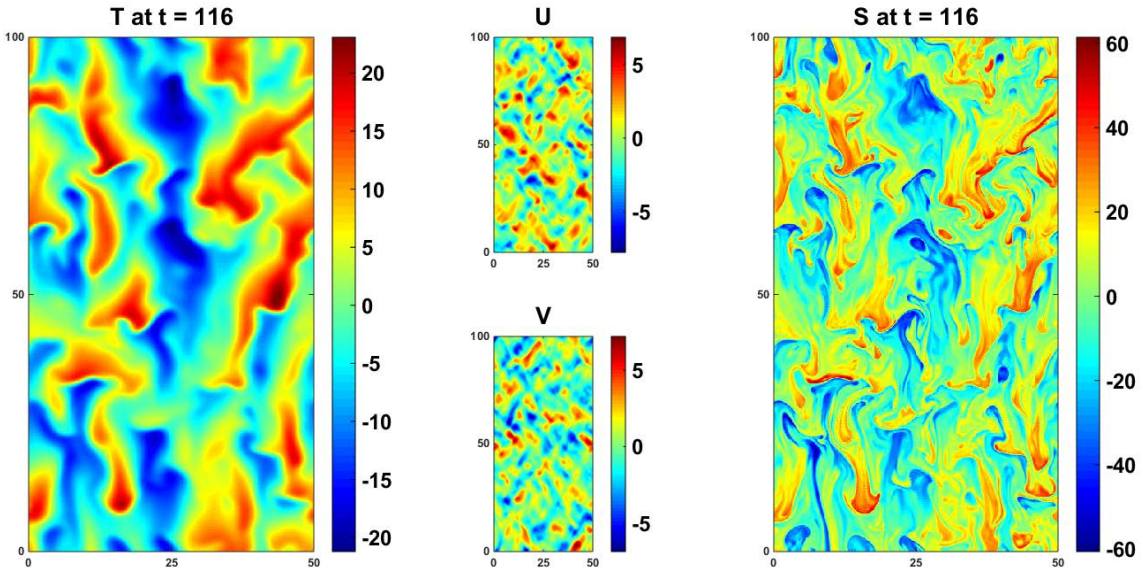

Figure 8. The baseline three-dimensional double diffusion simulation at time step 116 without induced velocity shear.

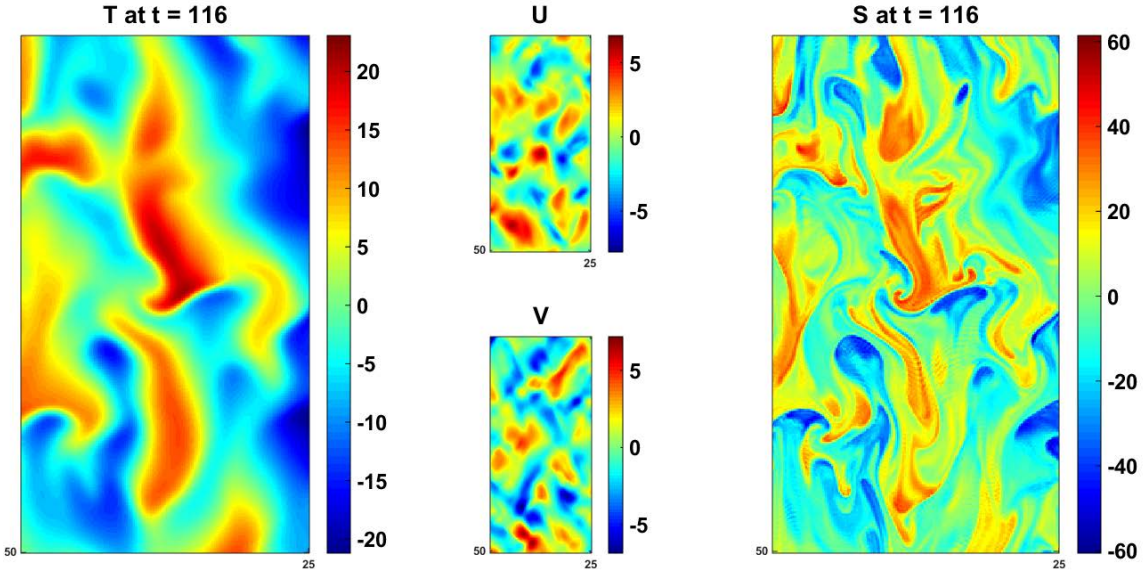

Figure 9. A magnified (2X) view of the baseline three-dimensional double diffusion simulation at time 116 without induced velocity shear.

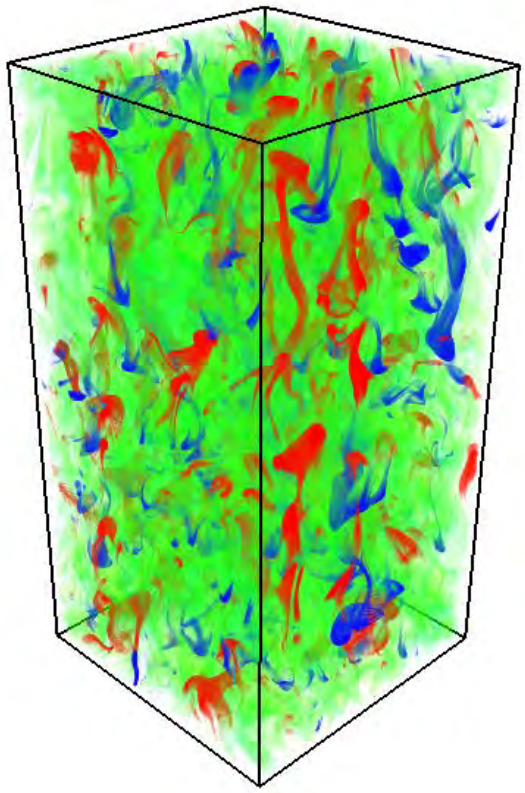

Figure 10. The baseline three-dimensional double diffusion simulation shown from the visualization software VAPOR.

The development of salt fingers from the baseline simulations and the resulting flux is shown in Figure 11. Upon development of salt fingers, the heat and salt flux rate stabilized to an equilibrium value. No external forces were in effect to disrupt or impact this steady state equilibrium. The resulting two-dimensional double diffusion flux values were approximately half the three-dimensional double diffusion values. The mean values for double diffusion following stabilization period are listed in Table 1. These values were used to determine how each modification to the base model affected double diffusion. The ratio of salt and heat flux is relatively constant. For simplicity, future graphs will display heat flux and tables will include the mean values of both heat and salt flux.

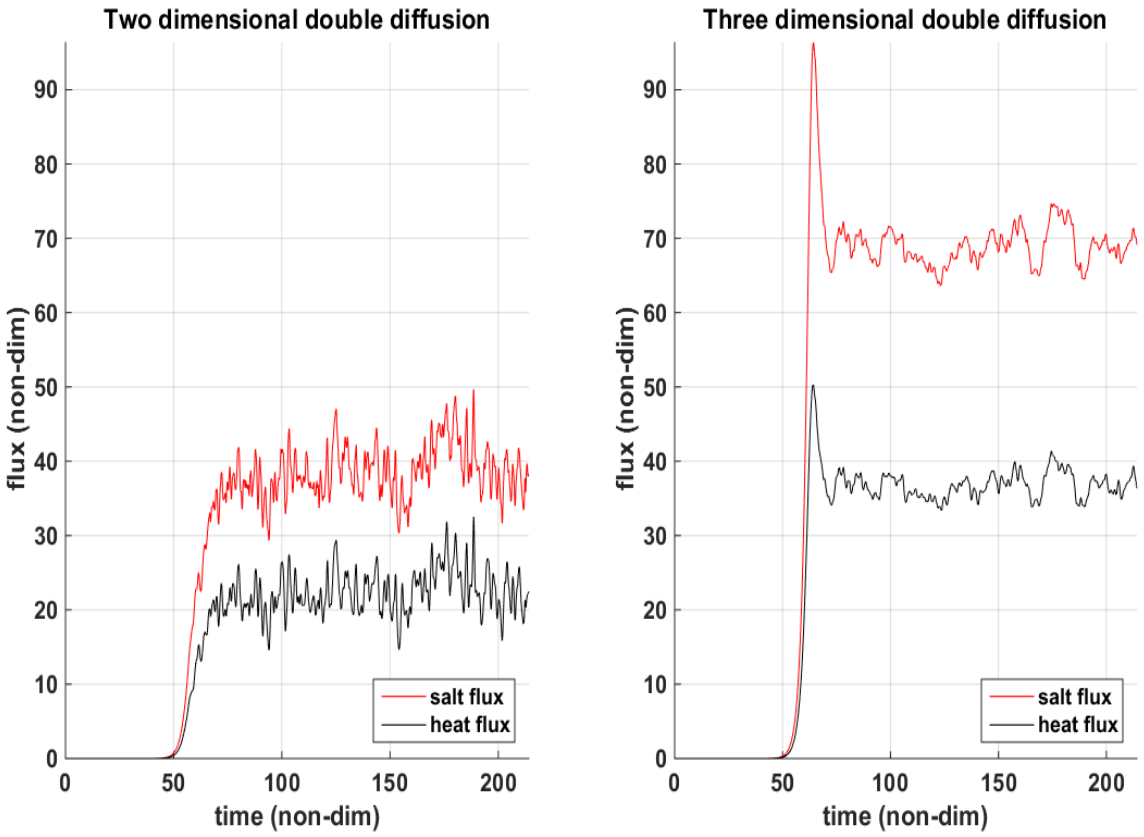

Figure 11. The two- and three-dimensional baseline reference values (non-dimensional units) for double diffusion without velocity shear.

Table 1. The complete results from the version one baseline model of two- and three-dimensional double diffusion models without velocity shear.

2-D Double Diffusion				3-D Double Diffusion			
Dimensional		Dimensionless		Dimensional		Dimensionless	
$\lvert F_H \rvert \left(\frac{watts}{m^2} \right)$	$\lvert F_S \rvert \left(\text{x}10^{-8} PSU \frac{m}{s} \right)$	$\lvert F_T \rvert$	$\lvert F_S \rvert$	$\lvert F_H \rvert \left(\frac{watts}{m^2} \right)$	$\lvert F_S \rvert \left(\text{x}10^{-8} PSU \frac{m}{s} \right)$	$\lvert F_T \rvert$	$\lvert F_S \rvert$
0.1373	5.118	22.805	39.165	0.2197	8.961	36.482	68.579

B. STEADY SHEAR SIMULATIONS

Double diffusion salt finger initiation under $R_i = 2$ is shown in Figure 12. This time step showed the strong induced velocity shear devoid of influence from salt finger projection.

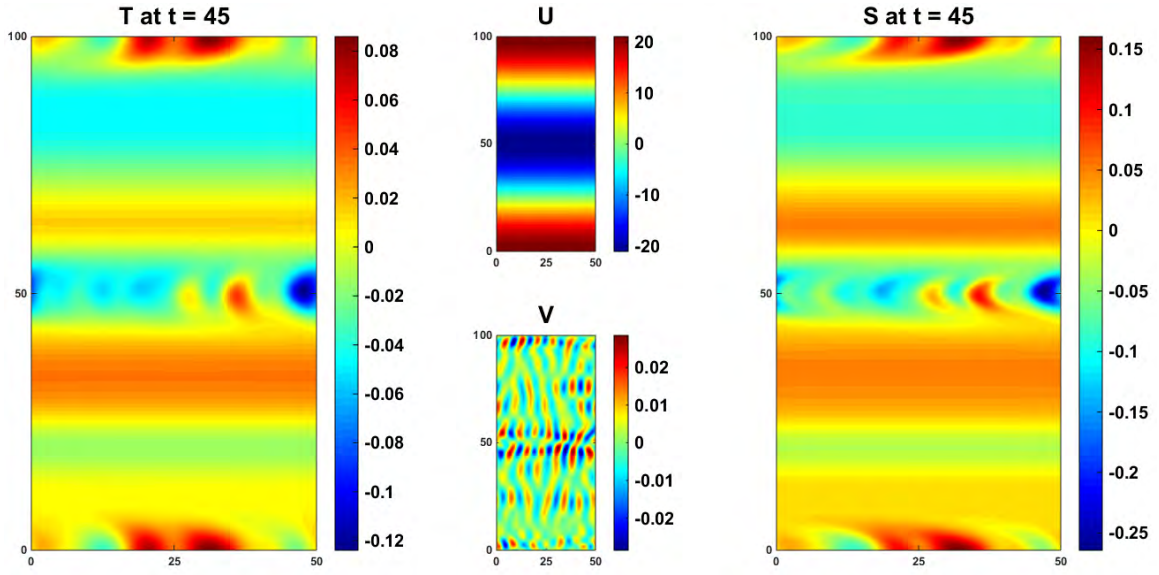

Figure 12. The initiation of salt fingers during the simulation using the version two non-rotational shear model for $R_i = 2$.

The same simulation is shown in Figure 13 at a later time step. This figure showed the salt finger structure alignment was influenced by the strong velocity profile. The formation and movement of salt fingers also introduced minor distortions to the velocity profile. The three-dimensional visualization in Figure 14 showed the same time step from orthogonal viewpoints. The image on the left showed the view of salt fingers cross-flow to the dominate shear. The salt fingers project vertically from this viewpoint, similar to the zero shear condition. The image on the right shows salt fingers aligned as sheets with clear structure formation impacted by the dominate shear.

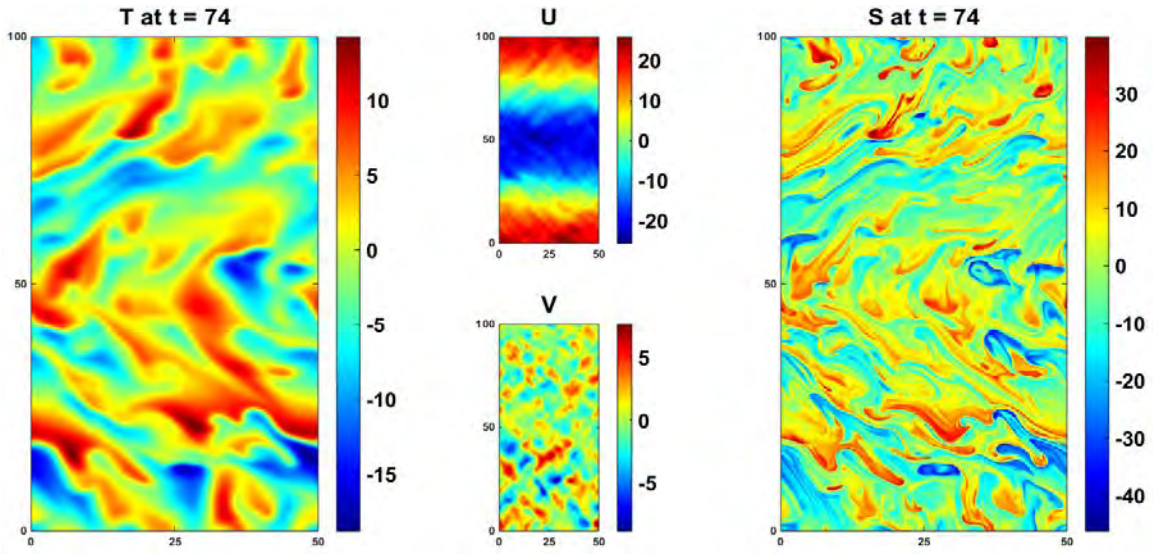

Figure 13. Fully developed salt fingers during the simulation using the version two non-rotational shear model for $R_i = 2$.

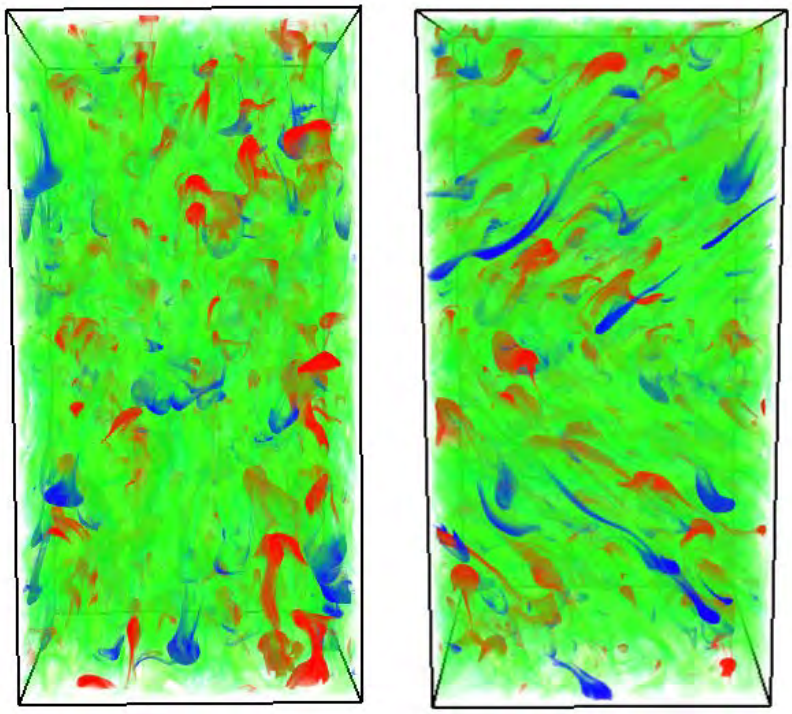

Figure 14. Salt finger structure from the simulation using the version two non-rotational shear model for $R_i = 2$. This shows the same time step from viewpoints offset by $90°$ to show impact from u and v velocity on salt finger structure.

The non-rotational three-dimensional velocity profile from $R_i = 2$ is displayed in Figure 15 at the onset of salt finger development. During this time step the strength of salt finger double diffusion is still low and hasn't affected the velocity profile. The three-dimensional visualization in Figure 16 showed salt finger alignment as influenced from shear in the u and v directions during the same time step. This velocity shear is incorporated over a vertical height of one meter. Despite this level of unrealistic shear over a small vertical height, the diffusion rates were not significantly impacted. Ocean conditions are not expected to have such drastic changes in current direction over a short vertical height. Therefore, diffusion rates in the ocean are expected to be impacted by spatial variability of shear even less than the results from this simulation.

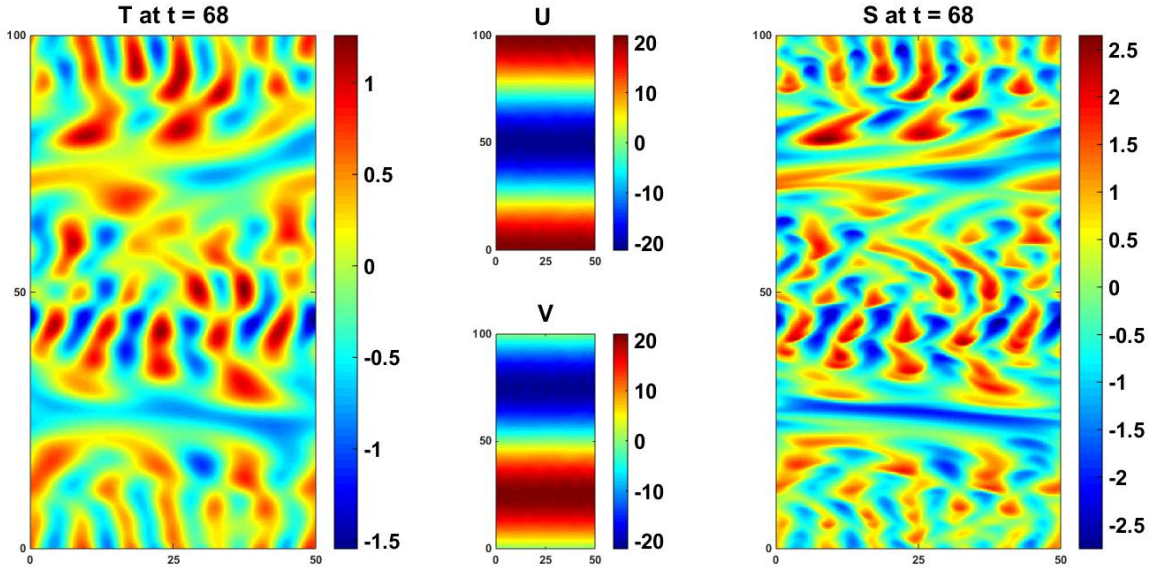

Figure 15. Initial salt finger development during the simulation using the version three non-rotational shear model for $R_i = 2$.

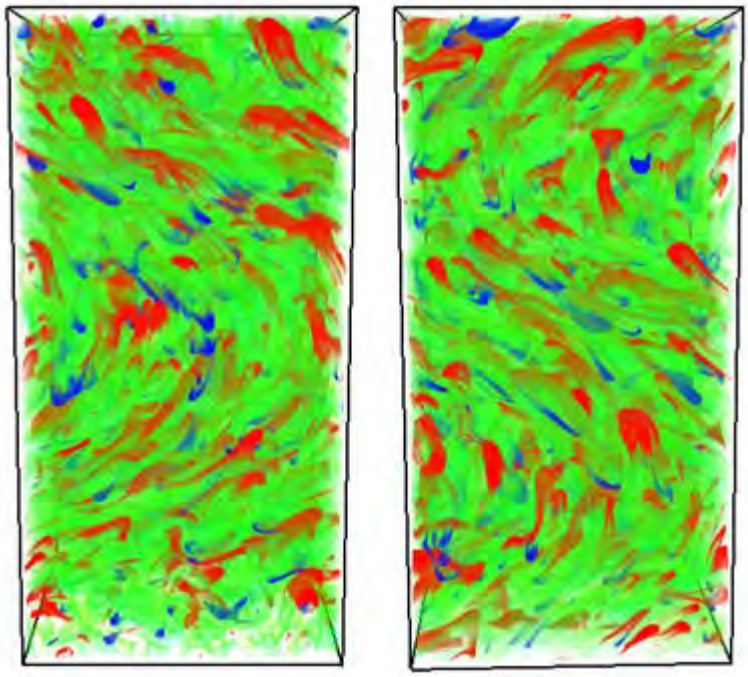

Figure 16. The version three non-rotational shear profile for $R_i = 2$, showing salt finger structure alignment from the dominate shear. This shows the same time step at viewpoints offset by $90°$, to show impact of u and v velocity shear on salt finger structure.

While shear undoubtedly affects fingers, it is interesting to note that the inverse is also true. Salt fingers introduced some distortion into the induced velocity profile as revealed by Figure 17, which shows three-dimensional salt fingers under $R_i = 2$ during a significantly advanced evolutionary stage (t = 353, ~ 60 hours real time). The minor distortion was still present in the velocity profile. This disturbance remained relatively constant and did not increase in strength over time to cause any appreciable instability. The effect of shear on salt finger alignment remained consistent during the non-rotational velocity profile part of model versions two and three.

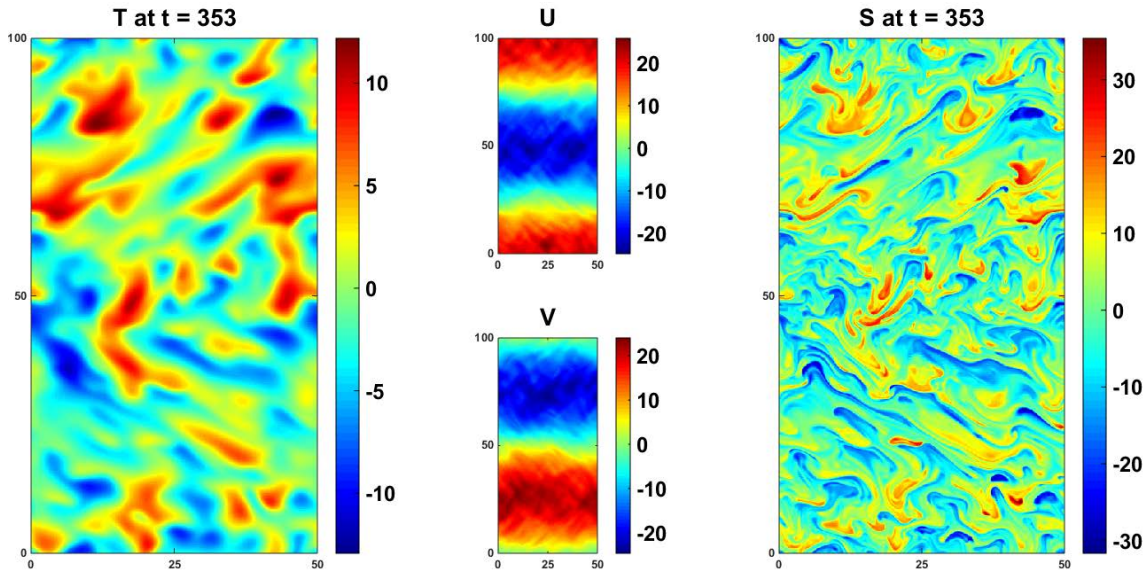

Figure 17. Salt finger structure during the version three non-rotational shear model for $R_i = 2$ after ~60 hours of real time.

Following stabilization, the resultant average heat fluxes for zero angular rotation are shown in Figure 18 for each value of R_i. The hindrance to vertical elongation of salt fingers as a result from the third version of the shear model did not translate to a significant reduction in overall double diffusion rates. Both velocity profile structures displayed an asymptotic approach toward the baseline three-dimensional heat flux reference value. The full results for model versions two and three are included in Table 2.

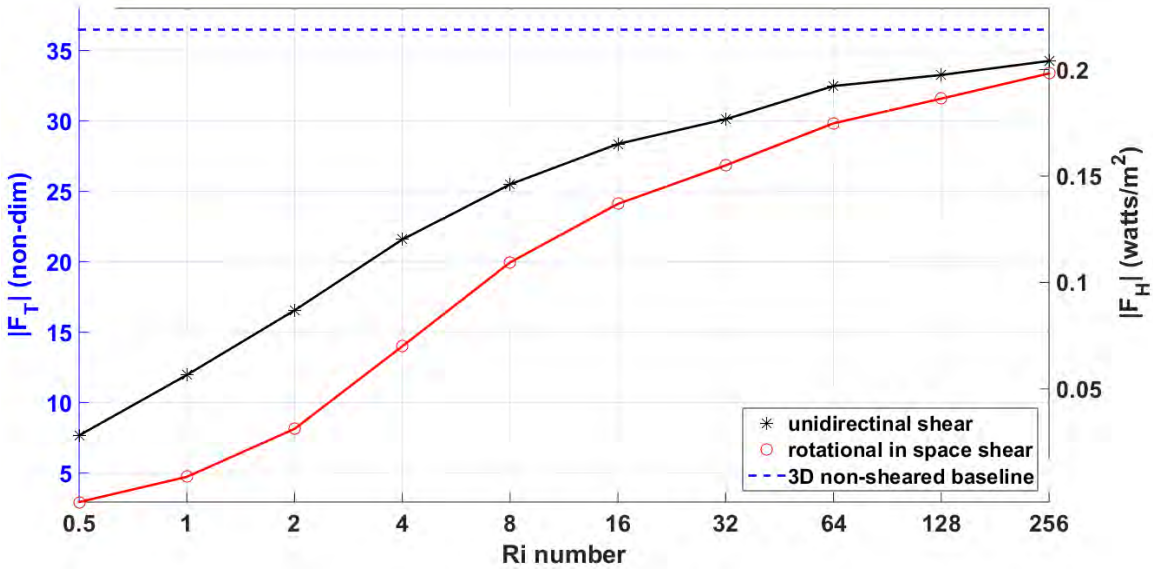

Figure 18. Mean temperature fluxes after stabilization between model versions two and three's non-rotational velocity profiles for each value of Richardson number. This is referenced to the baseline three-dimensional heat flux without velocity shear.

Table 2. The full resultant mean flux from the version two and three non-rotational shear models after stabilization has occurred.

	Version Two Unidirectional shear				Version Three Rotational in Space Shear			
	Dimensional		Dimensionless		Dimensional		Dimensionless	
R_i	$\lvert F_H \rvert$ $\left(\frac{watts}{m^2}\right)$	$\lvert F_S \rvert$ $\left(\text{x}10^{-8} PSU\,\frac{m}{s}\right)$	$\lvert F_T \rvert$	$\lvert F_S \rvert$	$\lvert F_H \rvert$ $\left(\frac{watts}{m^2}\right)$	$\lvert F_S \rvert$ $\left(\text{x}10^{-8} PSU\,\frac{m}{s}\right)$	$\lvert F_T \rvert$	$\lvert F_S \rvert$
0.5	0.0462	1.836	7.671	14.049	0.0177	0.7236	2.939	5.538
1	0.0720	2.871	11.964	21.974	0.0285	1.175	4.730	8.993
2	0.0996	4.062	16.542	31.086	0.0485	20.19	8.051	15.452
4	0.1300	5.330	21.587	40.790	0.0843	3.474	14.004	26.583
8	0.1536	6.321	25.505	48.372	0.1202	4.938	19.961	37.794
16	0.1708	7.078	28.371	54.166	0.1452	5.991	24.113	45.852
32	0.1814	7.542	30.124	57.717	0.1617	6.737	26.848	51.556
64	0.1956	8.093	32.481	61.939	0.1796	7.479	29.831	57.241
128	0.2003	8.088	33.265	63.428	0.1902	7.916	31.585	60.578
256	0.2063	8.518	34.261	65.186	0.2009	8.315	33.373	63.632

C. ADJUSTING THE PERIOD OF ROTATION

Rotational effects on double diffusion were determined during the second series of simulations using model versions two and three. To fully understand these effects, four simulations ran under a different period of rotation with a peak

velocity amplitude from $R_i = 0.5$ and $R_i = 2.0$. This also determined the effect on the range for instability of double diffusion while under the influence of different conditions of rotational shear.

1. Rotational Velocity Shear Under $R_i = 0.5$

Active salt finger formation was observed while under the effect of steady shear from $R_i = 0.5$ for both velocity profiles. Salt finger formation was observed for all four periods of temporal rotation considered for the version two shear rotational shear profile (T=0.5h, T=1h, …). Once spatial rotation was introduced version three shear profile, the results were inconclusive. The simulation recorded high levels of heat and salt flux for the three-dimensional velocity profile with a half-hour period of rotation. The level heat and salt flux decreased as the rate of rotation slowed. This was the opposite for how the version two shear model simulations performed. Closer examination of two- and three-dimensional visualization for the version three shear model simulations revealed additional instabilities. The complicated velocity pattern in this configuration produced new mixed dynamic / double-diffusive instabilities that contributed to vertical mixing of heat and salt. However, the simulation recorded the net vertical transport F_T and F_S. No attempt was made to separate traditional double diffusive mechanisms from the new dynamics introduced by rotating shear.

There seemed to be some sporadic salt finger formation during the simulations, however the heat and salt flux from double diffusion could not be isolated from flux by the potential destabilization induced by spatially rotating velocity. Figure 16 shows an advanced stage for the four hour period of rotation simulation on the version three shear model. The figure shows very low strength heat and salt flux and the structure of these bands show only a slight deviation from the horizontal plane. The rotational component applied to the velocity profile seemed to prevent salt finger development under the high velocity shear strength during this simulation. The overall results from these simulations are shown in

Table 3. The results from the version three shear model simulations appeared to be comprised mainly from turbulent action more than the result of double diffusion. These results are compared to the values obtained for the same velocity profile strength without induced rotation.

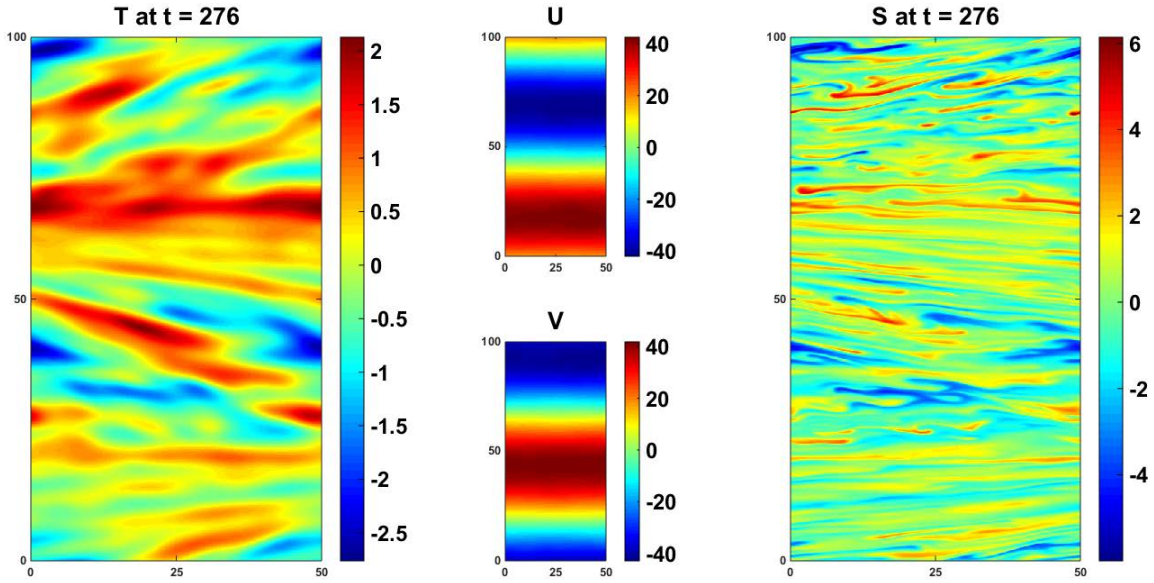

Figure 19. The version three shear model simulation for $R_i = 0.5$ and a period of rotation of four hours.

Table 3. The simulation results from the rotational part of model versions two and three for $R_i = 0.5$.

	Version Two $R_i = 0.5$				Version Three $R_i = 0.5$			
Period	Dimensional		Dimensionless		Dimensional		Dimensionless	
T (Hr)	$\lvert F_H \rvert$ $\left(\frac{watts}{m^2}\right)$	$\lvert F_S \rvert$ $\left(\text{x}10^{-8} PSU \frac{m}{s}\right)$	$\lvert F_T \rvert$	$\lvert F_S \rvert$	$\lvert F_H \rvert$ $\left(\frac{watts}{m^2}\right)$	$\lvert F_S \rvert$ $\left(\text{x}10^{-8} PSU \frac{m}{s}\right)$	$\lvert F_T \rvert$	$\lvert F_S \rvert$
0.5	0.0230	0.9692	3.822	7.417	0.0826	3.159	13.719	24.175
1	0.0268	1.141	4.456	8.733	0.0170	0.5807	2.827	4.444
2	0.0339	1.418	5.633	10.854	0.0162	0.5506	2.684	4.214
4	0.0385	1.588	6.393	12.156	0.0009	0.02927	0.155	0.224
∞	0.0462	1.836	7.671	14.049	0.0177	0.7236	2.939	5.538

2. Rotational Velocity Shear Under $R_i = 2$

The velocity profile strength of $R_i = 2$ was used to test rotational shear effects on double diffusion further with conditions further from the instability region. The developmental structure for salt fingers under the two-dimensional rotating velocity profile and a period of four hours is shown in Figures 20 and 21. Initial salt finger formation in Figure 20 seemed to be influenced by velocity shear. As the simulation progressed, this effect dissipates and the salt finger structure aligned with the vertical axis as shown in Figure 21. This characteristic alignment remained consistent over all four periods of rotation. There was a small drop in salt and heat flux once rotation was introduced into the two-dimensional velocity profile. After this initial drop, the different rates of rotation had a minimal effect on double diffusion rates. These results are listed in Table 4.

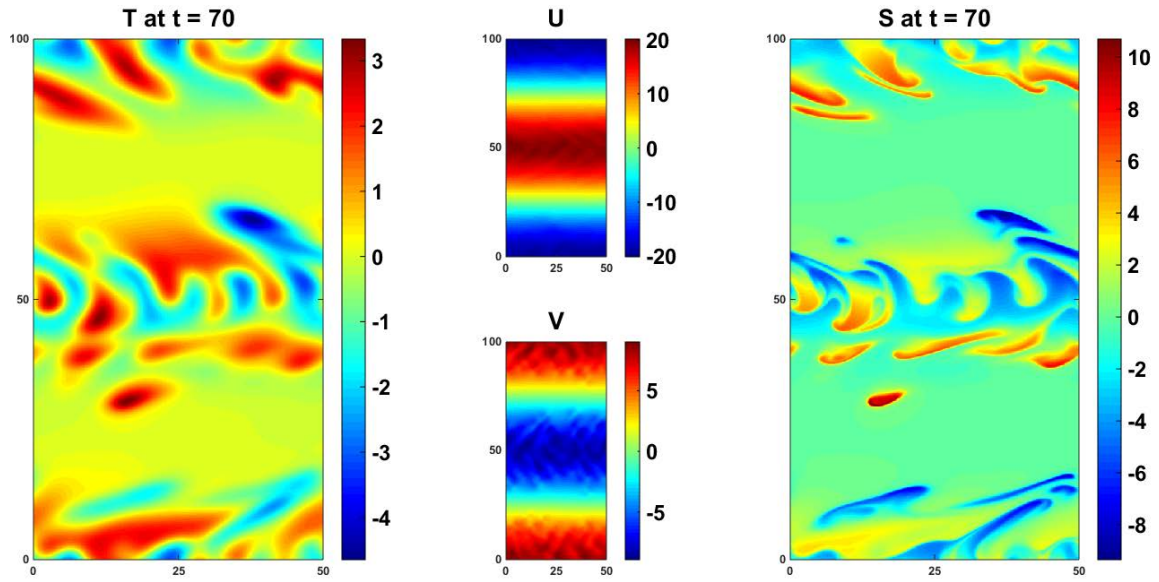

Figure 20. Salt finger initiation during the version two shear model simulation for $R_i = 2$ and a period of rotation of four hours.

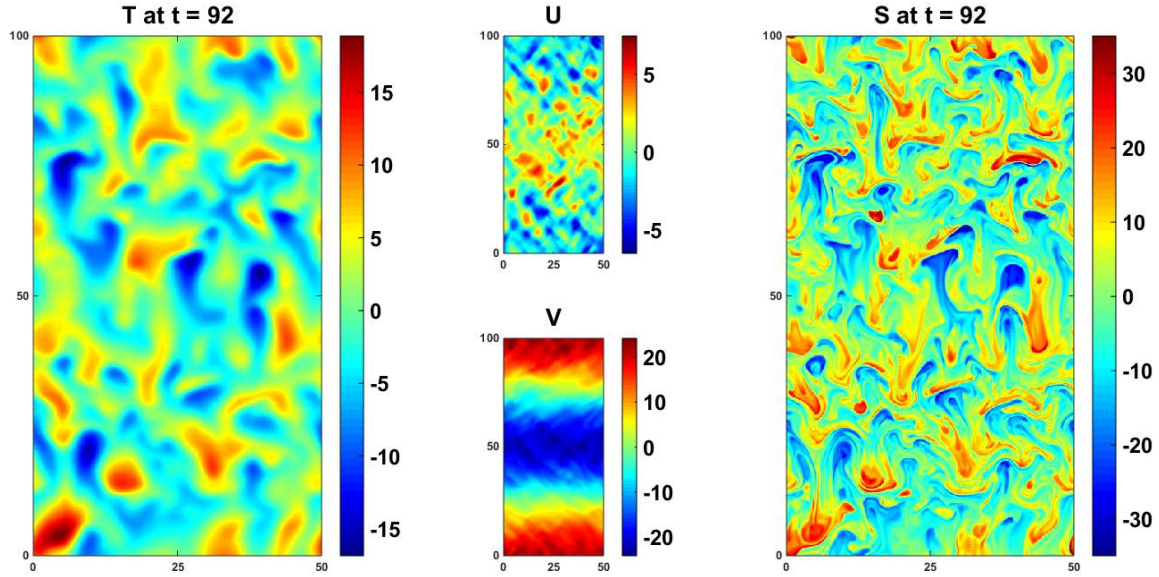

Figure 21. Fully developed salt fingers from the version two shear model for $R_i = 2$ and a period of four hours.

The same dynamic instabilities shown for $R_i = 0.5$ were present for three of the four $R_i = 2$ simulation runs. Salt finger formation was evident on all four simulations. For periods faster than four hours, the effect of double diffusion

appeared to be dominated the new instabilities associated with the rotational version three shear profile. When the period was slowed to four hours, salt finger formation occurred and appeared to only be minimally impacted from rotational vorticity. The formation of salt fingers for the four hour period of rotation on the three-dimensional velocity profile is shown in Figures 22 and 23. The structure of salt fingers was influenced by the induced shear. The averaged results from the simulations are shown in Table 4. All four periods of rotation had some contribution from cyclonic action. The four hour period of rotation was slow enough for the strength of the velocity profile, that this effect appeared to be minimal. This downward rotational vorticity can be seen in Figure 24.

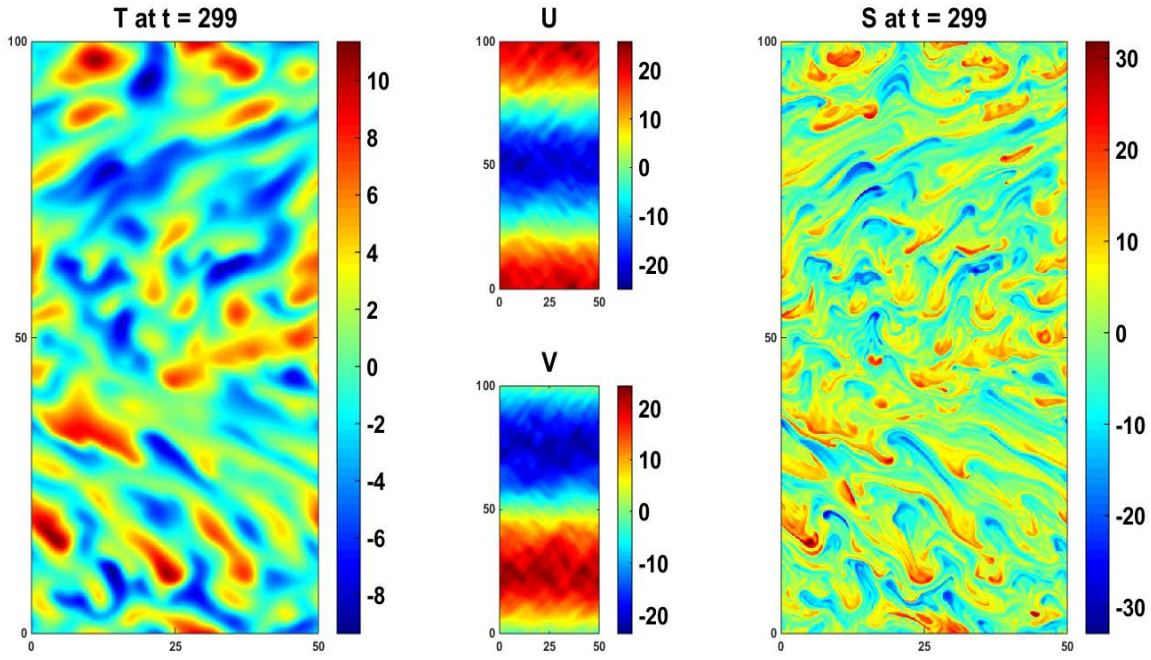

Figure 22. The impact of shear on salt finger structure during the version three shear profile for $R_i = 2$ and a period of four hours.

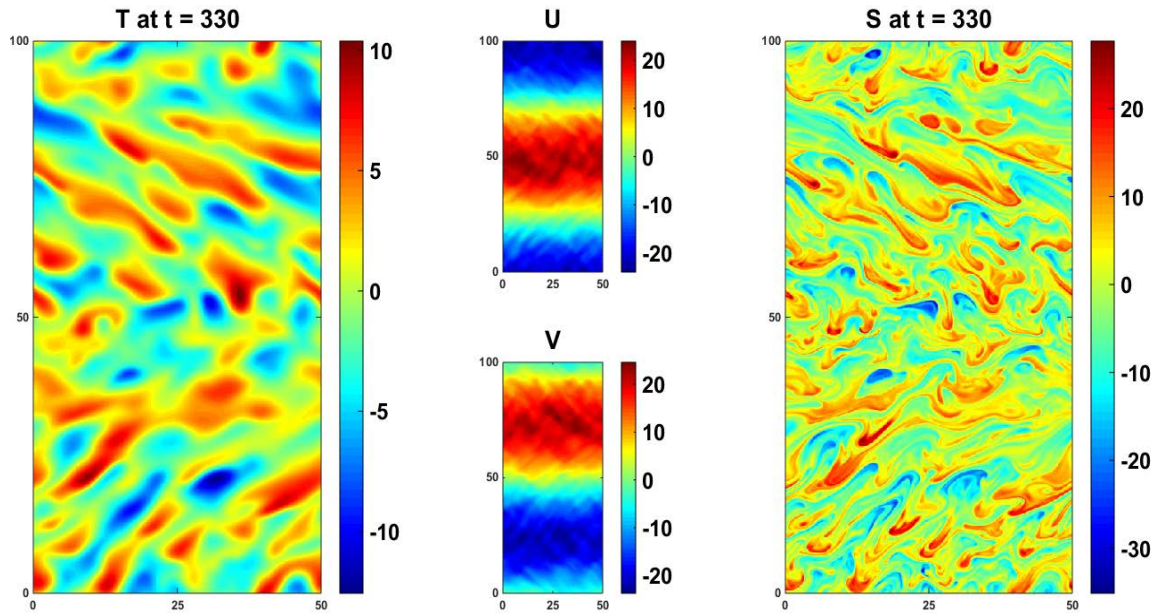

Figure 23. The impact of shear on salt finger structure during the version three shear profile for $R_i = 2$ and a period of four hours. This shows that the structure of salt fingers re-align as the direction of shear changes.

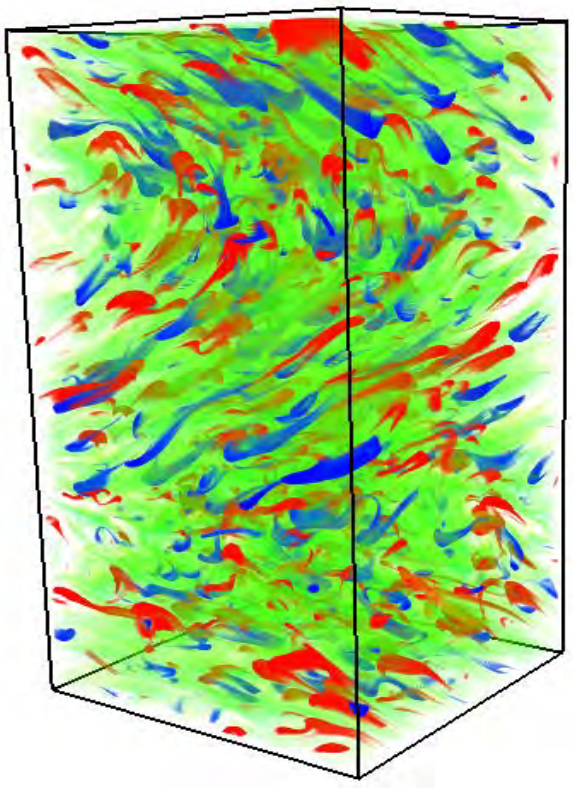

Figure 24. The simulation of version three shear model for $R_i = 2$ and a period of rotation of four hours. This showed the additional instabilities that contributed to the vertical transport of salt and heat.

Table 4. The simulation results from the rotational part of model versions two and three for $R_i = 2$.

	Version Two $R_i = 2$				Version Three $R_i = 2$			
Period	Dimensional		Dimensionless		Dimensional		Dimensionless	
T (Hr)	$\lvert F_H \rvert$ $\left(\frac{watts}{m^2}\right)$	$\lvert F_S \rvert$ $\left(\text{x}10^{-8} PSU \frac{m}{s}\right)$	$\lvert F_T \rvert$	$\lvert F_S \rvert$	$\lvert F_H \rvert$ $\left(\frac{watts}{m^2}\right)$	$\lvert F_S \rvert$ $\left(\text{x}10^{-8} PSU \frac{m}{s}\right)$	$\lvert F_T \rvert$	$\lvert F_S \rvert$
0.5	0.0947	3.911	15.726	29.933	0.1645	6.419	27.315	49.128
1	0.0926	3.833	15.374	29.333	0.0903	3.582	14.995	27.415
2	0.0911	3.909	15.133	29.918	0.0626	2.435	10.391	18.636
4	0.0935	3.845	15.527	29.425	0.0366	1.564	6.073	11.950
∞	0.0996	4.062	16.542	31.086	0.0485	2.019	8.051	15.452

THIS PAGE INTENTIONALLY LEFT BLANK

IV. RESULTS: STOCHASTIC SHEAR

The model versions two and three demonstrated how the strength of velocity shear and single frequency rotation impacted double diffusion salt and heat flux. However, a water column in the ocean is influenced by many wave frequencies of varied strength simultaneously. To understand salt finger formation under these conditions, a stochastic velocity shear was implemented into the DNS model. This full stochastic time series was then filtered to understand how different ranges of frequency impact double diffusion.

A. DOUBLE DIFFUSION UNDER AN UNFILTERED FREQUENCY TIME SERIES

The first simulation examined double diffusion under the stochastic velocity shear generated from the unfiltered frequencies that conformed to the GM frequency spectral model. During this stage of research, double diffusion rates don't stabilize into a single a steady state value, but fluctuate as a result from the oscillating velocity shear as a result of large low frequency components of the internal wave frequencies. This fluctuation is shown in Figure 25 as double diffusion rates made several oscillations from peak to trough. The resultant mean values cycled near the values obtained from the baseline two-dimensional zero shear double diffusion simulation. The mean heat flux from the full stochastic simulation is 73.70% of the two-dimensional baseline average while the mean salt flux is 81.77% of the two-dimensional baseline average.

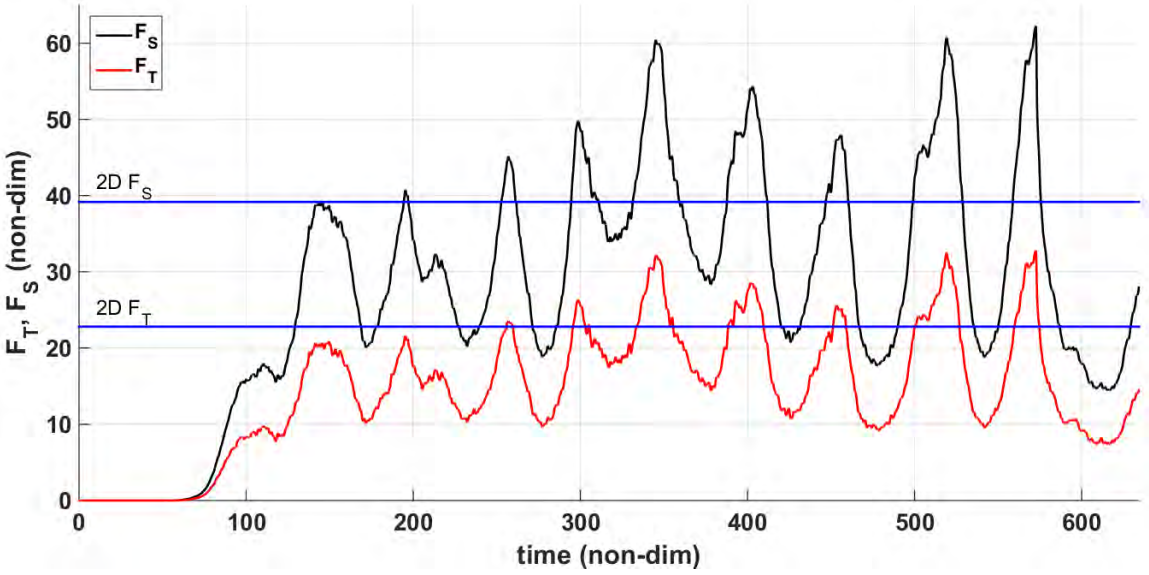

Figure 25. Double diffusion salt finger flux under the unfiltered GM frequency generated stochastic velocity shear time series. This is compared to the mean baseline two-dimensional double diffusion rates.

Figure 26 shows the initiation of double diffusion while under a stochastic velocity shear. A strong u velocity is shown during this time step in comparison to the weaker v velocity. Minor disruption of the velocity profile is evident when velocities are lower. This could be a result from velocity shear oscillation or the initial salt finger formation. Initial salt finger elongation was influenced by the velocity shear.

The stochastic velocity shear resulted in periods that cycled from strong velocity shear, to periods of reduced velocity shear within the water column. This resulted from different frequencies combining constructively and destructively to form the velocity shear. One period of minimal velocity shear is shown in Figure 27. These periods of weak and strong velocity shear caused the cyclic flux shown in Figure 25. The peak periods for double diffusion heat and salt flux occurred during a weak velocity shear while periods of low double diffusive flux occurred during periods of strong velocity shear.

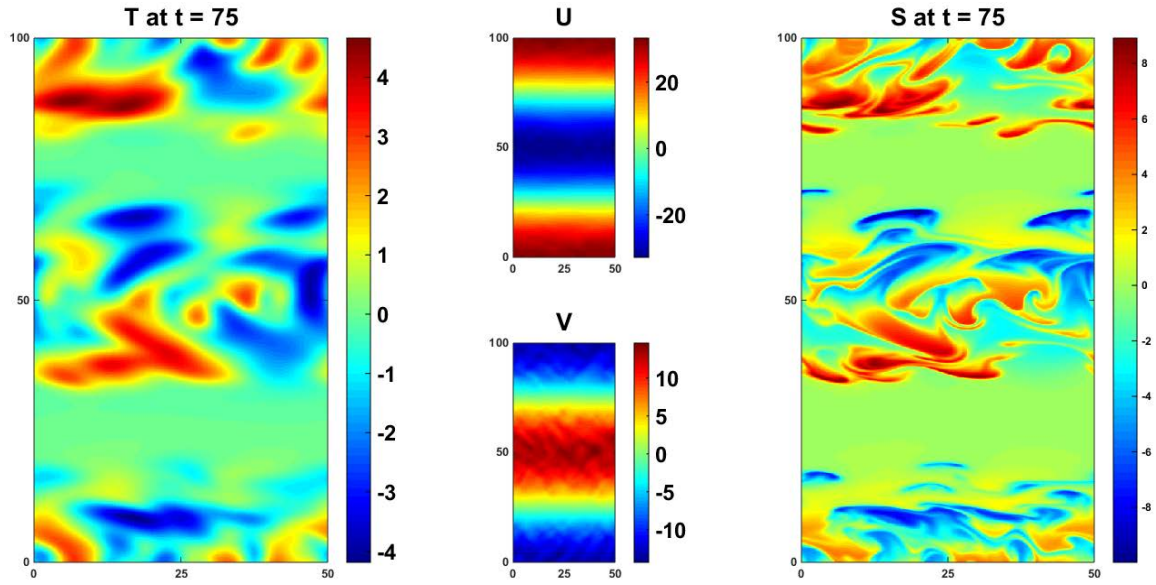

Figure 26. The initiation of salt finger development under the unfiltered stochastic velocity shear.

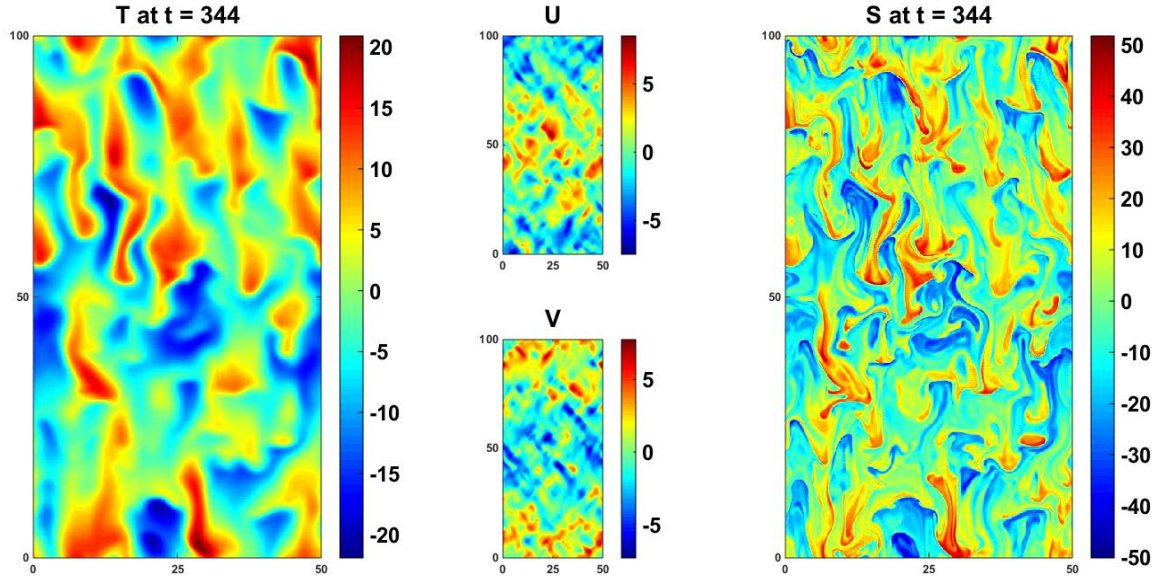

Figure 27. Salt finger structure alignment during a period of reduced velocity shear in the simulation of unfiltered stochastic velocity shear.

The relative relationship between heat flux and shear was determined as follows. The relative heat flux variation r_{fl} and relative variation in absolute shear r_{sh} was calculated by:

$$r_{fl} = \frac{F_T - \overline{F}_T}{\overline{F}_T}$$
$$r_{sh} = \frac{A_{sh} - \overline{A}_{sh}}{\overline{A}_{sh}} \qquad (2.20)$$
$$A_{sh} = \sqrt{\mathbf{u}_z^2 + \mathbf{v}_z^2}.$$

The relationship is shown in Figure 28 between $r_{fl}(t)$ and $-r_{sh}(t)$. Salt finger formation stabilized around time 100. Following this time, Figure 28 shows a strong correlation between these values. An increase or decrease in shear is rapidly followed by reduced or amplified vertical heat transport.

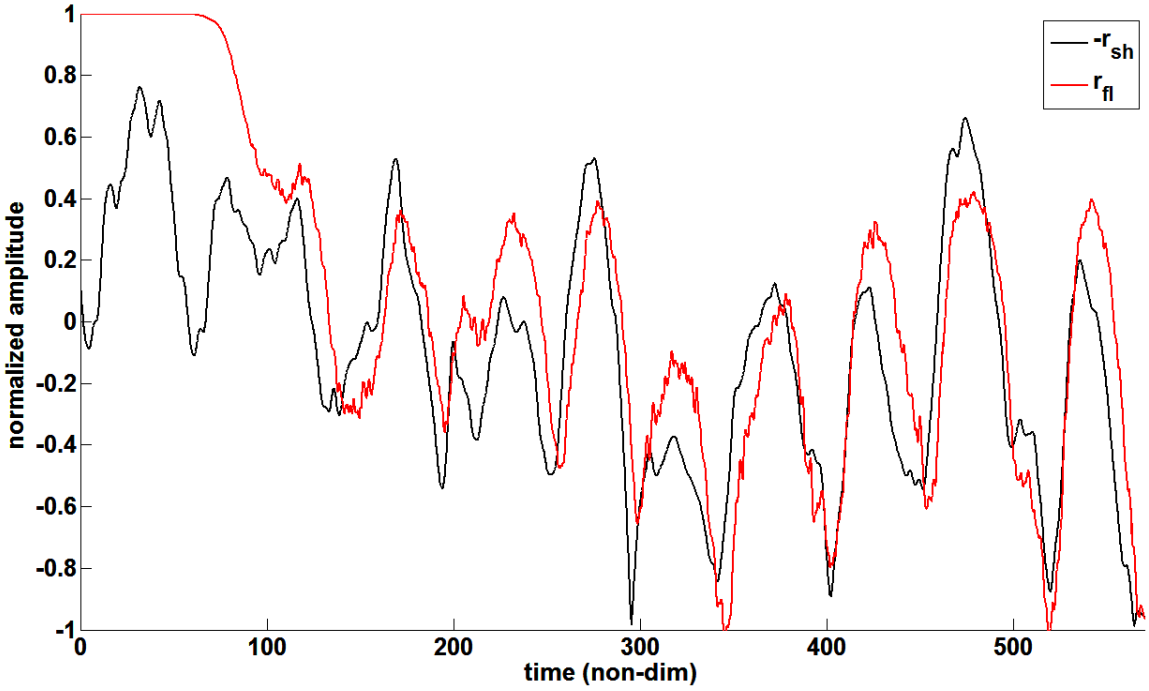

Figure 28. The correlation of $r_{fl}(t)$ and $-r_{sh}(t)$ from the unfiltered stochastic shear simulation.

B. DOUBLE DIFFUSION UNDER FILTERED FREQUENCY TIME SERIES

As expected, the overall structure of velocity shear is largely determined by the lower range of frequencies. The intermediate and high frequencies applied finer details to the overall structure velocity shear time series. The comparison of

frequency range impact on velocity shear against the unfiltered stochastic velocity shear was shown in Figure 7. The effect these filtered frequencies had on double diffusion is shown in figures 29 and 30. The low-pass filtered velocity shear resulted in higher velocity profiles and weaker flux in comparison to the other filtered results. The band-pass and high-pass filtered velocity shear time series resulted in a more weakly defined velocity profile and a subsequent stronger heat and salt flux. This is consistent with the variation in double diffusive flux shown from the full GM frequency generated velocity profile as well as the results from model versions two and three. The resultant double diffusion flux is shown in Table 5 for each simulation.

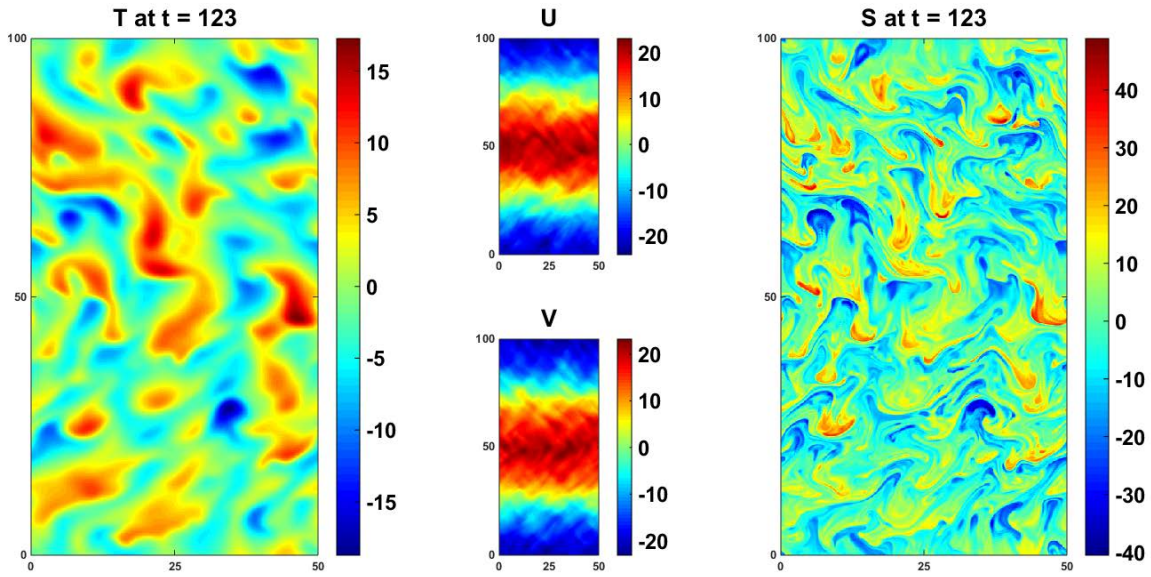

Figure 29. Salt fingers during the simulation for a low-pass filtered frequency generated stochastic velocity shear.

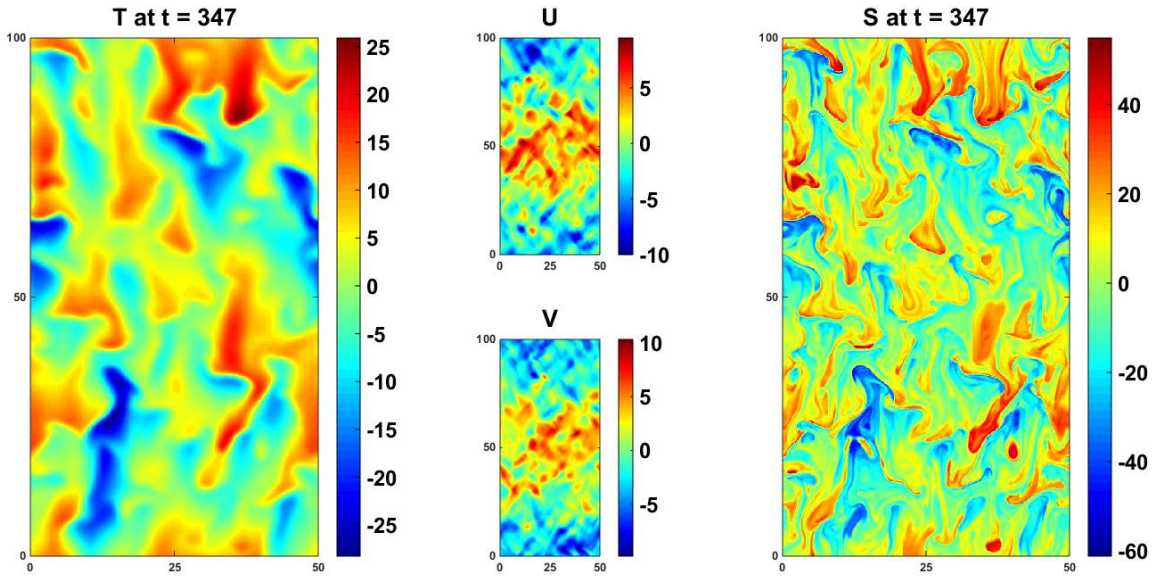

Figure 30. Salt fingers during the simulation for a band-pass filtered frequency generated stochastic velocity shear

Table 5. The resultant double diffusion salt and heat flux from each stochastic velocity shear time series simulation.

Frequencies in effect		Dimensional		Dimensionless	
		$\lvert F_H \rvert$ $\left(\frac{watts}{m^2}\right)$	$\lvert F_S \rvert$ $\left(\text{x}10^{-8}\, PSU\, \frac{m}{s}\right)$	$\lvert F_T \rvert$	$\lvert F_S \rvert$
Full	$(all\ \omega)$	0.1012	4.185	16.807	32.027
Low	$(\omega < f_1)$	0.1408	5.816	23.391	44.510
Intermediate	$(f_1 < \omega < f_2)$	0.1935	7.975	32.134	61.030
High	$(f_2 < \omega)$	0.2134	8.749	35.441	66.957

The temperature flux from each filtered velocity shear simulation compared to the original baseline two- and three-dimensional zero velocity shear simulations are shown in Figure 31. The low frequencies generate a strong velocity shear profile with fluxes comparable to the two-dimensional baseline results. The intermediate and high filtered frequencies resulted in a much weaker velocity profile and fluxes in these cases better approximate values from the baseline three-dimensional zero velocity shear. This indicates that low frequency

current oscillations are more disruptive to the formation and elongation of salt fingers than intermediate and high frequency current oscillations.

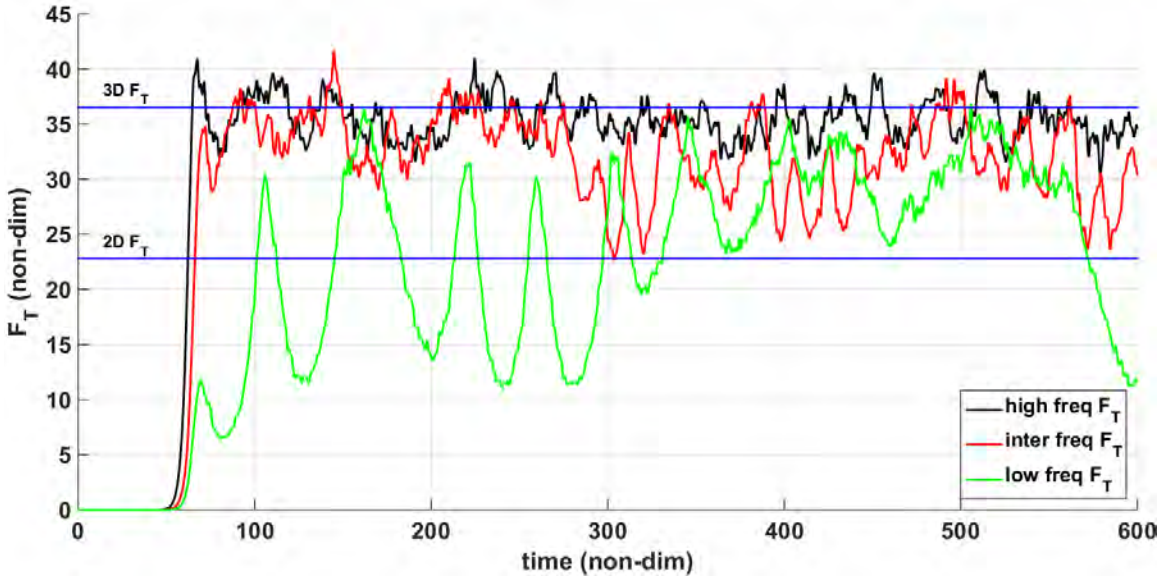

Figure 31. Temperature flux from the filtered stochastic velocity shear simulations compared to the baseline two- and three-dimensional temperature flux with zero velocity shear.

The impact that each velocity shear from the stochastic shear simulations had on salt finger alignment is shown in Figure 32. In this figure you can see that the shear from the unfiltered and low frequency filtered simulations had significant effect on salt finger alignment. The energies from the intermediate and high frequency simulations did not impact the alignment of salt fingers. This could be a result of the associated energies from those frequency ranges or the rate of frequency oscillation being too fast in comparison to salt finger time scales to result in structure alignment.

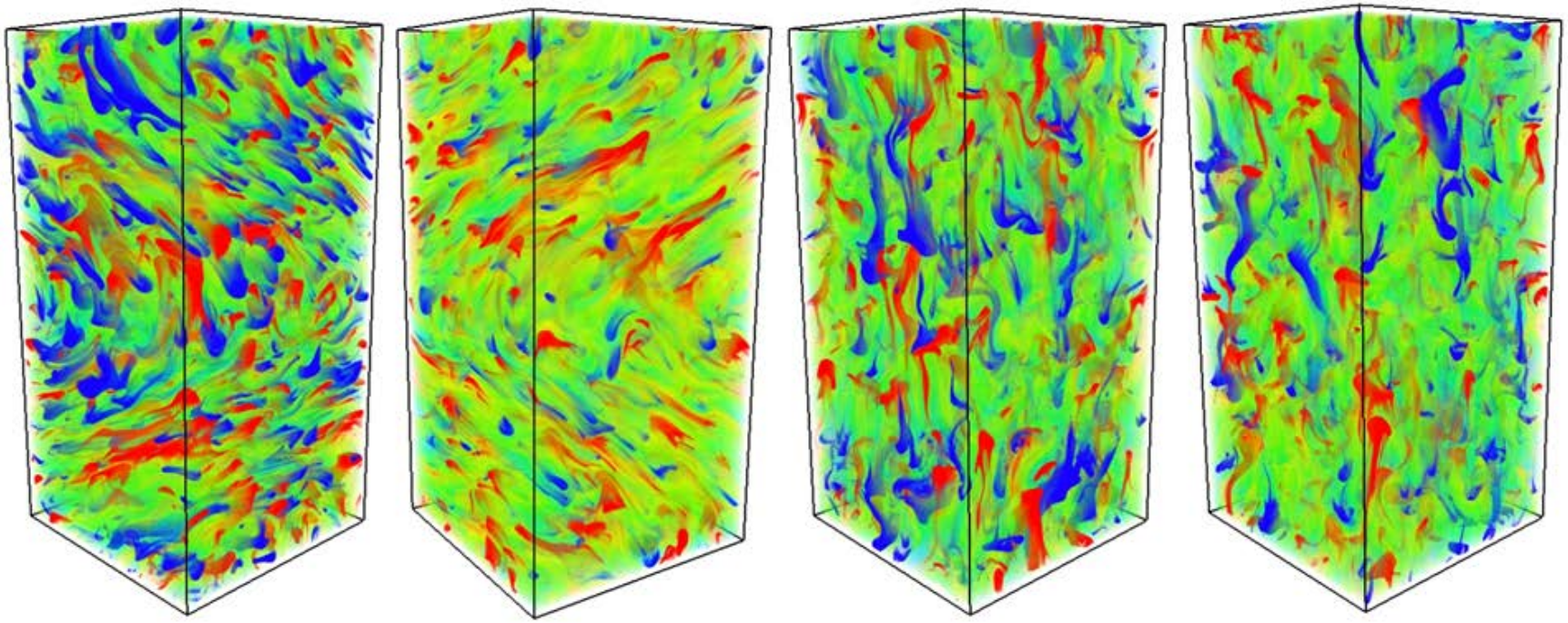

Figure 32. The influence from velocity shear on salt finger structure alignment during the stochastic velocity shear simulations. From left to right the figures represent shear from; unfiltered frequency forcing, low frequency filtered forcing, intermediate filtered frequency forcing, and high filtered frequency forcing.

V. CONCLUSIONS

This study examined the effect of various large-scale shears on the mixing rates and structure of salt fingers. The first parameter examined was the strength of velocity shear and the resultant impact on salt fingers. The second examination was the effect of a single frequency of rotation for two velocity profiles. Finally, the effect of a stochastic velocity shear was examined under various frequency ranges. Of primary interest was the impact of shear on the resultant salt and temperature flux. These results were compared with the baseline two- and three-dimensional salt finger simulations without velocity shear.

A. VARYING RICHARDSON NUMBER

Under a steady velocity shear, the strength of the shear has a direct impact upon salt finger formation and structure. For both a two- and three-dimensional velocity profile, the strength of the velocity shear has an inverse effect on the salt finger mixing rates. The resultant salt fingering was strongly influenced by both the direction and strength of velocity shear.

B. VARYING FREQUENCY

Unexpected results were obtained from inducing a single frequency period of rotation on the two velocity shear profiles. When $R_i = 0.5$, the parameter regime is sufficiently close to the dynamic instability range ($R_i < 0.25$) and the system behavior was somewhat erratic for either velocity profile. The experiments with unidirectional velocity profile were characterized by an increase in the intensity of salt fingering and double diffusion mixing rates as the rate of rotation slowed. The three-dimensional velocity profile simulation was too close to instability under the combined velocity shear strength and rates of rotation. During this simulation, salt finger formation was sporadic and the obtained salt

and heat flux appeared to be driven by instabilities associated with rotational vorticity rather than dominated by double diffusion.

The velocity shear for $R_i = 2$ are more favorable for salt finger formation. The unidirectional velocity profile simulation demonstrated a marginal decrease in diffusion rates once rotation was introduced. After rotation was initiated, the rates for double diffusion were fairly consistent and appeared to not be impacted by the rate of rotation. The three-dimensional velocity profile simulation formed salt fingers during each period of rotation. The combination of velocity shear strength, rate of rotation and the induced velocity profile still resulted in diffusion rates that could be attributed to the downward rotational vorticity that developed. During the simulation with a four-hour period of rotation, this effect was marginalized and the resultant salt and heat flux appeared to be largely representative for double diffusion salt fingers in the absence of shear.

The structure of the velocity profile in the third model version was unrealistic in terms of the vertical variability. Shear profiles in the ocean would have horizontal current flow would change direction over a much greater vertical height. This would result in a velocity profile more in accord with the model version two when comparing the scale of salt fingers to the overall velocity profile. The combined results from versions two and three indicate that rotation does not significantly impact the formation of salt fingers and the strength of salt flux and heat flux. The strength of the velocity shear does impact double diffusion rates to a degree, but does not preclude them from forming.

C. STOCHASTIC SHEAR

The implementation of a stochastic velocity shear profile helped determine if the results obtained from model versions two and three carried over into conditions more realistic to those found in the ocean. The clear correlation of velocity shear and resultant heat flux from Figure 24 showed the information obtained from the version two and three shear models remained relevant under stochastic conditions. A change in velocity shear would rapidly alter the

instantaneous rates of salt and heat flux. The shifting velocity shear would also result in a rapid realignment of salt finger structure as influenced by the direction of the shear.

The simulations for various filtered frequencies showed that the range of frequency does impact double diffusion. Lower frequencies result in higher velocity shear and a larger variation in this shear. This shear strongly influenced the structure of salt fingers and the wax and wane of the velocity shear results in a subsequent increase or reduction in double diffusion rates (Radko et al. 2015). Intermediate and high frequencies generate weaker velocity shear gradients which results in a weaker impact on the structure of salt finger and the resultant double diffusion rates (Radko et al. 2015).

The unfiltered and low filtered stochastic time series simulation results approximated the baseline two-dimensional simulation for zero shear conditions. The intermediate and high frequency filtered simulation results were similar to the results of the baseline three-dimensional zero shear simulation. The unfiltered three-dimensional stochastic velocity shear simulation only differed from the baseline two-dimensional simulation by 26.3% for temperature flux and 18.23% for salt flux. This information is very useful for future research. The simulation runtime for a stochastic shear three dimensional double diffusion simulation would require in excess of 75,000 computer hours to resolve fully. A two-dimensional double diffusion simulation without shear could be fully resolved for a small fraction of the computational cost. This would result in approximately a 25% reduction in accuracy, but would reduce the computational runtime by two orders of magnitude.

D. NAVAL RELEVANCE

Double-diffusion affects the effectiveness of hydrodynamic-based detection techniques. A better understanding of the effects of shear on double diffusion could help analyze for the passage of bodies through the water. Some studies have already been conducted to test the distortion of thermohaline

staircases and the channel propagation of acoustic signals (Bulters, 2013). Other areas of concern could be how better parameterization of the ocean microstructure could affect the accuracy of operational numerical large-scale models of ocean circulation (Radko 2013). In each of these instances, a clearer understanding of the small-scale dynamics of double diffusion would improve the rests of these applications.

APPENDIX

Table 6. Base DNS model inputs

Name	Value
De-aliasing	True
Precision	Single
X extent of the box	50
Y extent of the box	50
Z extent of the box	100
Max degree of x Fourier modes	128
Max degree of y Fourier modes	128
Max degree of z Fourier modes	256
Temperature gradient	0.01
Salinity gradient	0.01
Thermal buoyancy parameter	7
Compositional diffusion coefficient	7
Thermal diffusion coefficient	1
Compositional diffusion coefficient	0.01
Thermal stratification parameter	1
Compositional stratification parameter	0.5
Initial time step length	$5*10^{-5}$
Maximum time step length	$3*10^{-2}$
CFL safety factor	0.9

THIS PAGE INTENTIONALLY LEFT BLANK

LIST OF REFERENCES

Bulters, A. C., 2012: Three-dimensional structure of thermohaline staircases in the tropical north Atlantic and their effect on acoustic propagation.

Colosi, F. A., and M. G. Brown, 1998: Efficient numerical simulation of stochastic internal-wave-induced sound-speed perturbation fields, *J. Accoust. Soc. Am.*, **103**, 2232–2235.

Fernandes, A. M., and R. Krishnamurti, 2010: Salt finger fluxes in a laminar shear flow, *Cambridge University Press*, **658**, 148–165.

Garrett, C. and W. Munk, 1972: Space-time scales of ocean internal waves. *Geophys. Fluid Dyn.*, **2**, 225–264.

Huppert, H. E., and J. S. Turner, 1981: Double-diffusive convection. *J. Fluid Mech.,* **106**, 299-329.

Kimura, S. and W. Smyth, 2007: Direct numerical simulation of salt sheets and turbulence in a double-diffusive layer, *Geophysical Research Letters*, **34**, 1–5.

Kunze, E., 1990: The evolution of salt fingers in inertial wave shear, *J. Mar. Res.*, **48**, 471–504.

Kunze, E., 1994: A proposed flux constraint for salt fingers in shear. *J. Mar. Res.*, **52**, 999–1016.

Kunze, E., A. J. Williams III, and R. W. Scmitt, 1987: Optical microstructure in the thermohaline staircase east of Barbados, *Deep Sea Res.*, **34**, 1697–1704.

Levine, M. D., 2002: A Modification of the Garrett-Munk Internal Wave Spectrum, *Journal of Physical Oceanography*, **32**, 3166–3181.

Linden, P. F., 1974: Salt Fingers in a Steady Shear Flow, *Geophysical Fluid Dynamics*, **6**, 1–27.

Lvov, Y. V. and E. G. Tabak, 2001: Hailtonian formalism and the Garret-Munk spectrum of internal waves in the ocean, *Physical Review Letters,* **87**, 1–4.

Munk, W., 1981: Internal waves and small-scale processes, *The Evolution of Physical Oceanography*, 264–291.

Radko, T., 2013: *Double-Diffusive Convection*, Cambridge University Press, 344pp.

Radko, T., J. Ball, J. Colosi, and J. Flanagan, 2015: Double-diffusive convection in a stochastic shear, *Journal of Physical Oceanography*, submitted.

Radko, T. and M. E. Stern, 1999: Salt fingers in three dimensions, *Journal of Marine Research*, **57**, 471–502.

Ruddick, B., and O. Kerr, 2003: Oceanic thermohaline intrusions: Theory. *Progress in Oceanogr.*, **56**, 483–497.

Schmitt, R. W., 1994: Double diffusion in oceanography, *Ann. Rev. Fluid. Mech.*, **26**, 255–285.

Schmitt, R. W., 1995: The Ocean's salt fingers, *Scientific American*, **272**, 70–75.

Schmitt, R. W., 1995: The Salt Finger Experiments of Jevons (1857) and Rayleigh (1880), *J. Phys. Oceanogr.*, **25**, 8–17.

Stellmach, S., A. Traxler, P. Garaud, N. Brummell, and T. Radko, 2011: Dynamics of fingering convection II: The formation of thermohaline staircases. *J. Fluid Mech.*, **677**, 554–571.

Stern, M. E., 1969: Collective instability of salt fingers. *J. Fluid Mech.*, **35**, 209–218.

Stern, Melvin E., 1960: The "salt-fountain" and thermohaline convection, *Tellus.*, **12**, 172–175.

Stern, M. E., T. Radko, and J. Simeonov, 2001: 3D salt fingers in an unbounded thermocline with application of the Central Ocean, *J. Fluid Mech.*, **67**, 554–571.

Stommel, H., A. B. Arons, and D. Blanchard, 1956: An oceanographical curiosity: The perpetual salt fountain. *Deep Sea Res.*, **3**, 152–153.

St. Laurent, L. and R. W. Schmitt, 1999: The contribution of salt fingers to vertical mixing in the North Atlantic tracer release experiment, *J. Phys. Oceanogr.*, **14**, 599–611.

Turner, J. S., H, Stommel, 1964: A new case of convection in the presence of combined vertical salinity and temperature gradients, *Proc. Natl. Acad.* **52**, 49-53.

INITIAL DISTRIBUTION LIST

1. Defense Technical Information Center
   Ft. Belvoir, Virginia

2. Dudley Knox Library
   Naval Postgraduate School
   Monterey, California